OPEN GEOMECHANICS

In situ X-ray CT imaging of transient water retention experiments with cyclic drainage and imbibition

Marius Milatz [a], **Edward Andò** [b],
Gioacchino Viggiani [c] **& Serge Mora** [d]

[a] *Hamburg University of Technology (TUHH), Institute of Geotechnical Engineering and Construction Management*

[b] *École Polytechnique Fédérale de Lausanne (EPFL), EPFL Center for Imaging, Lausanne, Switzerland*

[c] *Univ. Grenoble Alpes, CNRS, Grenoble INP, 3SR, 38000 Grenoble, France*

[d] *Université de Montpellier and CNRS, Laboratoire de Mécanique et Génie Civil, Montpellier, France.*

Abstract. The water retention curve (WRC) represents a key function in unsaturated soil mechanics as it can be applied for the modeling of the hydro-mechanical behaviour of unsaturated soils. The macroscopic WRC is characterised by different phenomena, such as hysteresis upon cyclic drainage and imbibition. With the help of modern X-ray computed tomography and hydraulic experiments that can be performed in a CT scanning environment, so-called *in situ* CT experiments, we image cyclic drainage and imbibition in a sand on the pore scale in order to quantitatively measure and study the change of microstructure and *capillary state variables*, characterising capillary effects in unsaturated granular soils. The measured pore scale data can then be related to the macroscopic WRC. To our knowledge, for the first time very different *capillary state variables*, such as interfacial areas, contact lines and contact angles, could be extensively measured in high detail for various hydraulic cycles in our experiment. Besides the experimental procedure, the wealth of measured data will be comprehensively presented and discussed and finally shared with the research community.

Keywords. Unsaturated granular soils, Water retention behaviour, Transient flow experiments, X-ray computed tomography
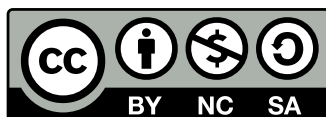
1. Introduction

1.1. Water retention behaviour of granular media

Fundamentals of capillarity

Granular soils, such as sands, characterise a large part of the Earth's surface in most countries. Therefore, they represent an important natural building ground and material in geotechnical engineering. Due to the availability of water in the porous system of surface-near soils, originating from ground water or precipitation, a large portion of natural soils is generally unsaturated, *i. e.*, neither fully dry nor water saturated, and thus influenced by capillary effects.

In a natural capillary system, on which we focus in this contribution, water forms the so-called wetting phase, while air represents the nonwetting phase. The wetting properties of a fluid or gas depend on their contact angle θ with regard to a contacting surface or other medium. If the contact angle is less than 90 degrees, a fluid is called wetting. If the contact angle is larger or equal, the fluid is nonwetting, with the fluid surface being repelled by the contacting surface.

Starting from the water saturated state of a soil in which the soil grains are completely immersed in water, a gradual decrease of water content leads to the formation of capillary menisci at the interface of air and water in a specific contact angle. With further decreasing water content, the wetting phase becomes disconnected until water clusters and isolated capillary bridges build up, connecting single grains and transferring capillary forces on the microscopic level. These forces originate from the interfacial tension γ, also known as surface tension for thermodynamic equilibrium and chemically pure fluids [Blunt, 2017], inside the air-water interfacial area of the menisci and represent a contribution to effective stress in the unsaturated state. For water $\gamma = 0.07275$ N/m at 20°C.

On a macroscopic level, the capillary forces acting inside the interfaces of two immiscible fluids in a porous medium lead to capillary rise of pore water above the ground water table. In this hydraulic domain, pore water pressure is negative and equal to the capillary pressure that can be derived from the capillary rise. This capillary pressure p_c is also called soil suction, or more concrete, matric suction s if only the portion caused by capillarity within the porous soil matrix is considered [Fredlund and Rahardjo, 1993]. Matric suction is then given as the difference of the pore air pressure u_a and pore water pressure u_w inside the soil according to Eq. 1.

$$s = u_a - u_w, \tag{1}$$

If the pore air pressure is equal to atmospheric pressure which is set to zero as a reference pressure, matric suction is equal to negative pore water pressure.

The link between macroscopic pore water and pore air pressure or capillary pressure and microscopic interfacial tension and capillary forces inside a single capillary of radius r is derived from the Young–Laplace law, given by Eq. 2.

$$p_c = u_a - u_w = \frac{2\gamma \cos\theta}{r} \tag{2}$$

The equation results from vertical force equilibrium of the water meniscus in a capillary tube. θ is the contact angle between wetting fluid and solid surface. The capillary pressure p_c represents the pressure difference of pore air pressure u_a and pore water pressure u_w on both sides of the capillary membrane.

With the help of the definition of the radius of curvature of the meniscus R inside a thin tube as well as the relationship $r = R\cos\theta$, Eq. 2 can be transformed to the more general Eq. 3 allowing to calculate capillary pressure p_c or matric suction s from interfacial tension γ and a capillary curvature $\frac{1}{R}$.

$$p_c = u_a - u_w = \frac{2\gamma}{R} \tag{3}$$

In a more general three-dimensional case where the capillary meniscus is not spherical, mean curvature $H = \frac{1}{R_1} + \frac{1}{R_2}$, with R_1 and R_2 being the radii of mean curvature, is applied to calculate capillary pressure according to Eq. 4.

$$p_c = \gamma H = \gamma \left(\frac{1}{R_1} + \frac{1}{R_2} \right) \tag{4}$$

Microscopic origins of the macroscopic WRC

Due to the characteristic pore size distribution which is itself influenced by density, grain shapes, and grain size distribution, a soil volume encounters a multitude of different capillary pressures on the microscale, resulting in a macroscopic capillary pressure as the averaged effect for the whole considered soil volume. On this macroscopic level, the microscopic capillary effect leads to a measurable water retention curve when degree of saturation is plotted *vs.* capillary pressure or matric suction. An exemplary water retention curve of a sand is shown in Fig. 1. Its features will be explained in detail in the following.
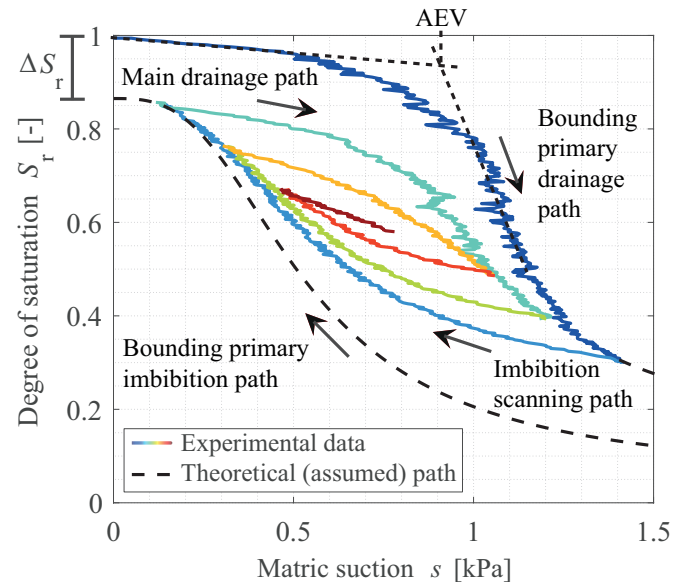

Figure 1. Water retention curve of a medium coarse to coarse grained sand with different consecutive hydraulic paths measured with the method proposed in Milatz [2020].

Open Geomechanics, 2022, article no. 5
Marius Milatz, Edward Andò, Gioacchino Viggiani & Serge Mora, *In situ X-ray CT imaging of transient water retention experiments with cyclic drainage and imbibition*

2

The characteristic S-shaped water retention curve is believed to reflect the drainage and imbibition phenomena happening on the microscale. The entire saturation range is typically divided into three different regimes depending on the availability and local distribution of pore water. In the capillary regime where the pores are still filled with water, however, with occluded air bubbles under natural conditions, an increase in matric suction leads to air entry upon primary drainage. When the macroscopic matric suction overcomes the capillary resistance for air entry, the so-called air entry value (AEV) is reached, and the pores begin to empty, with air entering from the top of the soil. When drainage continues, connected pore channels begin to further fill with air, creating a network of pore air volumes and vice-versa disconnected water clusters, which is called the funicular regime. At very low saturations, capillary bridges of isolated pore water in between single grains are formed, which is called the pendular regime. As these water menisci can be hardly driven out of the grain skeleton by a further increase in suction, a theoretical residual saturation S_{res} is frequently observed for water retention curves at very high matric suction. However, this saturation can be expelled by a full drying of the soil, *e. g.*, in an oven.

The mechanisms of drainage, as described above, occur on the so-called primary drainage path of a soil, starting from full water saturation. When a consecutive imbibition process takes place, a different macroscopic hydraulic path in the s-S_r space is measured, leading to the hysteresis effect of the macroscopic water retention curve that was described for the first time by Haines [1930]. Hysteresis leads to a hydraulic path-dependence in unsaturated soils, with hydraulic history developing between a bounding primary drainage and a bounding primary imbibition path as shown in Fig. 1. Upon reversal of the flow direction, a multitude of so-called drainage and imbibition scanning paths can be observed, with the hydraulic state in the s-S_r space asymptotically approaching the bounding primary drainage or primary imbibition paths. Closed scanning cycles of drainage and imbibition take the shape of ellipses as shown in Fig. 1. Owing to the hysteresis effect, the hydraulic history of a soil must be known in order to accurately describe its current hydraulic state as different suction levels exist for the same degree of saturation on the different hydraulic paths.

Due to air entrapment on the microscopic level, the full water saturation is usually not reached again when matric suction becomes zero upon imbibition, leaving a gap ΔS_r which is illustrated in Fig. 1. Different theoretical microscopic mechanisms of air entrapment are described in Bear [1979] and Lins [2009]. Essentially, air can get entrapped by the effect of bypassing when water flows around air clusters, leaving them locked inside smaller voids or in dead ends. The effect of entrapped air is believed to be one microscopic reason for the existence of hysteresis [Bear, 1979]. After air entrapment, a further drainage event leads to the so-called main drainage curve that runs asymptotically into the bounding primary drainage curve. A further known source of hysteresis is the non-uniform pore size distribution in

many soils. With the help of a pore space model that resembles to an ink-bottle, idealising a non-uniform pore space with small pore necks and larger pore bodies, different degrees of saturation for drainage and imbibition at the same matric suction can be explained. Due to the higher suction required to empty a water filled pore by air entering through a small pore neck compared to the lower suction required to fill a pore through its larger pore body, higher degrees of saturation are encountered on drainage paths compared to imbibition paths. This source of hysteresis in porous media due to the individual contributions of different pore sizes is usually referred to as the "ink-bottle effect" [Haines, 1930].

Another theoretical explanation for hysteresis, leading to different capillary pressure or matric suction for the same degree of saturation at drainage and imbibition, can be seen in different contact angles between pore water and solid grains, which is known as contact angle-hysteresis. Experiments on single droplets moving on an inclined plane indicate differences between the contact angles of an advancing and a receding fluid droplet θ_{adv} and θ_{rec}, with $\theta_{rec} < \theta_{adv}$ [de Gennes et al., 2004]. In accordance with Eq. 2, this observation leads to a higher capillary pressure or matric suction for a receding water meniscus upon drainage compared to an advancing meniscus upon imbibition inside the same capillary. As a consequence, the radii of meniscus curvature are different, with smaller radii of curvature for drainage and larger radii for imbibition processes.

Based on thermodynamics considerations, Hassanizadeh and Gray [1990] and Hassanizadeh and Gray [1993] argue that the hysteresis effect might be due to only considering the WRC as a functional relationship between degree of saturation and capillary pressure without taking a dependence on interfaces into account. By considering the air-water interfacial area as an additional state variable, it was shown based on experimental data and simulations that representative state surfaces can be obtained in the space, see Porter et al. [2009]. This would confirm the theoretical thermodynamical considerations about the hysteresis of the WRC, but it is still not clear how a unique functional relationship for the WRC based on the named and maybe even other variables can be established.

In agreement with Eq. 2, soil compaction leads to a decrease in void space and a reduction of average capillary radius which results in generally higher capillary pressures. Therefore, the water retention curve shows a density- or void ratio-dependence, with higher capillary pressures and higher AEVs measured for lower void ratios.

Traditionally, water retention curves are measured and modelled for static flow conditions. Accordingly, the aforementioned contact angles θ represent static contact angles. Due to viscous and dynamic effects, the static contact angle of a wetting fluid on a surface might be changed for fast flow events. Therefore, also so-called dynamic contact angles are measured in material sciences. The difference of dynamic and static contact angles represents an explanation for transient flow effects leading to transient or dynamic water retention curves [Diamantopoulos and Durner, 2012, Hassanizadeh et al., 2002]. These water retention curves can be measured for non-equilibrium flow conditions and

Open Geomechanics, 2022, article no. 5
Marius Milatz, Edward Andò, Gioacchino Viggiani & Serge Mora, *In situ X-ray CT imaging of transient water retention experiments with cyclic drainage and imbibition*

3

generally deviate from static soil water retention curves. If the flow rate is low enough, transient water retention curves and static water retention curves become the same.

1.2. Experimental investigation of the WRC

Many different laboratory experiments have been developed for the measurement of the WRC. Due to varying suction ranges in coarse and fine grained soils, different methods for the application of matric suction and measurement of water content or degree of saturation have been developed. An overview of different frequently used lab methods is given by Vanapalli et al. [2008].

Focusing on granular soils, such as sands, with a typical low suction range below 100 kPa or one atmosphere of negative pore water pressure that can occur under natural conditions, methods to control negative pore water pressures are frequently applied for suction control. In order to measure the equilibrium water retention curve, the hanging water column method [ASTMD6836-16, 2016] is frequently applied. According to this method, matric suction in the form of a negative water head is applied to a specimen through a porous filter plate with a defined AEV in different suction steps. For every suction step, the pore water outflow until equilibrium is measured in order to calculate the specimen degree of saturation. The reconstruction of the WRC by equilibrium s-S_r-data is labour-intensive and time-consuming because the unsaturated flow requires more equilibrium time with decreasing specimen degree of saturation. Especially for the investigation of higher-order scanning paths, an experiment may have to run for several weeks.

Another approach for the measurement of the WRC is given by the vice-versa procedure of changing the specimen water content or degree of saturation by application of forced pore water flow and measuring the corresponding response of specimen matric suction with the help of an embedded tensiometer sensor. With the help of such flow cell-based methods, transient quasi-static or dynamic water retention curves can be measured, depending on the applied flow rate [Milatz, 2015, 2020, Milatz et al., 2018a,b, Mirzaei and Das, 2013, Zhuang, 2017]. The first author's work on this field has led to the development of a miniaturised flow cell apparatus for the automated continuous measurement of transient WRCs of granular media, discussed in Milatz [2020], which is used for the CT experiments to be presented in this contribution.

Several authors have already applied X-ray computed tomography for the investigation of the WRC from a microscopic point of view [Higo et al., 2015, Khaddour, 2015, Khaddour et al., 2018, Kido et al., 2020, Manahiloh and Meehan, 2017, Thakur et al., 2020]. In many experiments, the hanging water column method was used to apply different levels of matric suction and degree of saturation to the investigated specimens. After equilibration of degree of saturation, CT images have been taken to analyse the microscopic phase distribution for different hydraulic states. Furthermore, microscopic interfacial properties, as given by the interfacial areas or curvature of menisci, have already

been measured using X-ray CT by Wang et al. [2019] or synchrotron-based CT by Armstrong et al. [2012], Culligan et al. [2004], Schlüter et al. [2016]. Contact angles were measured manually by Andrew et al. [2014] and by Manahiloh and Meehan [2017]. An automatic approach to contact angle measurement based on algorithmic processing of multiphase image data was presented by AlRatrout et al. [2017].

In order to achieve good contrast in images of multiphase materials, different techniques can be applied. In addition to image processing methods used after image acquisition, such as de-noising and filtering, the image contrast can already be enhanced during imaging by special experimental and imaging techniques. For a better contrast of water, dopants such as iodine, can be added, increasing its density and therefore contrast in X-ray images [Wildenschild et al., 2005, 2002]. Furthermore, the X-ray energy can be set in a way to cause the maximum absorption which is characteristic of the applied dopant. Especially when using synchrotron-based imaging, propagation-based phase contrast in conjunction with phase retrieval algorithms can be considered to enhance the contrast at phase boundaries for media with different refraction indices. Finally, neutron radiation can be applied on a stand-alone basis or combined with X-rays [Kim et al., 2013]. In contrast to X-rays, neutrons are mainly attenuated by atomic nuclei and allow to achieve strong contrast for hydrogen-containing materials which is very useful for the imaging of water in geomaterials [Tengattini et al., 2021].

1.3. Motivation and open research questions

In this contribution, *in situ* flow experiments are conducted in an X-ray CT scanner in order to obtain insights into the unsaturated flow behaviour on the pore scale. The CT data in between different hydraulic drainage and imbibition steps of the WRC that is also measured on a macroscopic level allows to track the fluid phases air and water and to evaluate different microscopic properties in order to shed light onto the different theoretical microscopic phenomena leading to the macroscopic realisation of the WRC. Furthermore, a better understanding of the WRC on the pore scale is also believed to improve our understanding of effective stress in a capillary system. Principal questions of research that guide us during the design of experimental procedures and analysis of CT data are the following:

1) Can the theories of microscopic origin of hysteresis be confirmed?
2) Which phase distributions and fluid structures develop during cyclic drainage and imbibition?
3) How do microscopic *capillary state variables*, such as the interfacial areas, the length of the contact line or contact angles as potential ingredients of effective stress, develop upon different hydraulic paths?

2. Material and methods

Open Geomechanics, 2022, article no. 5
Marius Milatz, Edward Andò, Gioacchino Viggiani & Serge Mora, *In situ X-ray CT imaging of transient water retention experiments with cyclic drainage and imbibition*

4

2.1. Tested material

Based on previous CT-based studies, a medium coarse to coarse grained natural sand referred to as "Hamburg Sand" and used as a model sand at Hamburg University of Technology is investigated here. The sand has been washed to remove particles smaller than 0.063 mm. Furthermore, ionoare containing particles that could lead to metal artifacts in CT images have been removed as good as possible using a strong magnet. A selection of different soil parameters is given in Tab. 1. The grain size distribution curve is shown in Fig. 2.

Table 1. Selected soil parameters of Hamburg Sand.

ρ_s [g/cm^3]	$e_{\min}$ [-]	$e_{\max}$ [-]	d_{10} [mm]	d_{50} [mm]	$d_{\max}$ [mm]
2.64	0.52	0.805	0.45	0.68	2.0

ρ_s: grain density, $e_{\min}$: min. void ratio
$e_{\max}$: max. void ratio
d_{10}: grain diameter at 10% passing
d_{50}: grain diameter at 50% passing
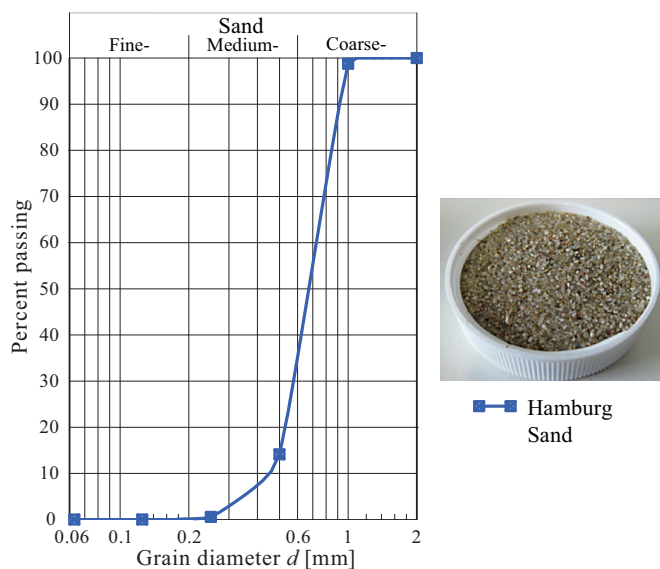$d_{\max}$: max. grain diameter

Figure 2. Grain size distribution curve of the tested Hamburg Sand and photograph of dry granular material.

As shown in a previous study [Milatz, 2020], the investigated sand exhibits low capillarity with an air entry value in the order of magnitude of 1 kPa, but with pronounced hysteresis and air entrapment which can also be noted by the WRC illustrated in Fig. 1.

2.2. Experimental set-up

For the *in situ* experiments in the CT system at Laboratoire 3SR, Université Grenoble Alpes (UGA) [Viggiani et al., 2015], the set-up for hydraulic experiments presented in Milatz [2020] was adapted to be placed on the rotation stage in between X-ray tube and detector screen as shown in Fig. 3.
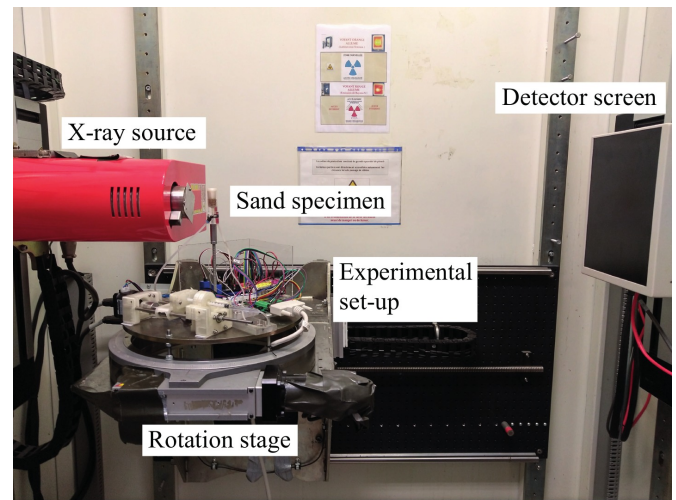

Figure 3. Experimental set-up inside the CT chamber at Laboratoire 3SR, Université Grenoble Alpes.

The experimental set-up, described in detail in Milatz [2020], consists of a miniature syringe pump with a clamped 1 ml-syringe for drainage and imbibition of the specimen as well as a system of two pore water pressure sensors for the measurement of matric suction in the drainage system underneath a filter plate supporting the sand specimen inside its flow cell. The whole experiment is controlled by a Raspberry Pi single-board computer, named the UNSAT-*Pi* 2, which runs a Python script for test- and CT scan-control. Different functions control the macroscopic change of degree of saturation inside the specimen by the syringe pump and the logging of suction data from the pore water pressure sensor. A schematic drawing of the experimental set-up and its most important technical components is shown in Fig. 4.
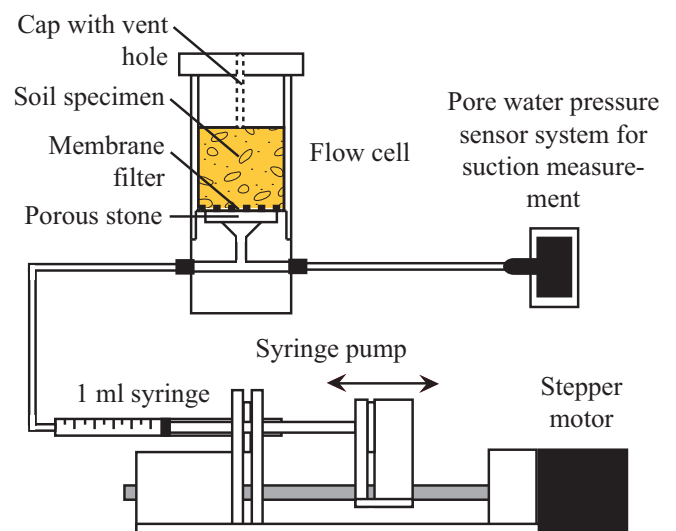

Figure 4. Schematic drawing of the experimental set-up to be placed in the CT scanning environment at Laboratoire 3SR.

For the application in a CT scanning environment, the original experimental set-up, presented in Milatz [2020], had to be modified by substituting all cable connections

between the Raspberry Pi and the control units for syringe pump and pore water pressure sensor by a curling 25-pin D-Sub cable. This cable connects the single-board computer, placed on the floor of the leaden X-ray cabin, to the experimental set-up on the rotation stage, allowing for a flexible data transfer and a minimisation of measurement disturbance by rotational movement.

2.3. Specimen preparation

Initially water saturated sand specimens are created by pluviating the selected dry mass of sand into the already water-filled cylindrical container with an inner diameter of 12 mm. The sand is carefully poured in with a small spoon using a small funnel, taking care that no single sand grain is lost. The specimen holder is filled in layers, each a few millimetres thick, that are carefully compacted and afterwards roughened with the tip of a screw driver to avoid the formation of segregated layers. This procedure is followed until the desired initial macroscopic specimen height of $h_0 = 12$ mm is reached. In order to also minimise air entrapment, the water level inside the specimen holder is always kept above the top of each sand layer. During specimen preparation, the pore water pressure is already logged to make sure that the measurement is working fine.

Prior to the first CT scan, the excess water on top of the sand specimen is slowly pumped out with the help of the syringe pump until the water level is located on top of the uppermost sand grains. Before the start of the CT scan, a topcap with a central aeration bore hole as shown in Fig. 4 is carefully pushed down on top of the specimen to fix it against grain movements and to minimise the effect of evaporation during the CT experiments.

The sand specimen was prepared in such a way to reach the initial macroscopic specimen properties presented in Tab. 2, corresponding to the state of other specimens investigated in previous research.

Table 2. Initial macroscopic specimen properties.

m_d [g]	V_0 [cm^3]	e_0 [-]	w_0 [-]	S_{r0} [-]
2.1711	1.3572	0.650	0.2462	1.0

m_d: dry mass, V_0: initial specimen volume
e_0: initial void ratio, w_0: initial gravimetric water content
S_{r0}: initial degree of saturation

2.4. Testing procedure during CT imaging

The Python code for controlling the hydraulic experiment presented in Milatz [2020] was enhanced by a feedback function for communication with the X-ray tomograph. This procedure allowed to automatically start a CT scan after the termination of each hydraulic step by having the Raspberry Pi check the presence of a status file via network connection. After the end of each CT scan, the Python program would continue with the next hydraulic step. With this approach, the step-wise hydraulic experiment with intermediate CT scans could be fully automated.

The selected experiment on a specimen of Hamburg Sand, presented in this contribution, consists of 19 hydraulic steps and 20 CT scans of different hydraulic states, including the initial water saturated specimen. Due to the automated testing procedure, all experimental stages could be performed in the same time steps.

Starting from the water-saturated initial state, 5 hydraulic steps on the primary drainage path were applied. They were followed by 4 steps on a 1st scanning imbibition path, 3 steps on a main imbibition or 1st drainage scanning path (after air entrapment), 2 steps on a 2nd imbibition scanning path, 2 steps on a 2nd drainage scanning path, 2 steps on a 3rd imbibition scanning path, and one last step on a 3rd drainage imbibition path. With every change in flow direction, the amplitude of total macroscopic saturation change ΔS_r was reduced in order to obtain always different scanning paths, leading to a whirl-shaped WRC. Fig. 5 shows the applied change in pore water volume ΔS_r during tomography steps and hydraulic steps during the whole experiment. The different macroscopic steps of pore water volume change have been selected in that way as to obtain the same saturation levels on different hydraulic paths to compare the microscopic capillary states at the same macroscopic saturation, but on different hydraulic paths. Thus, we focus especially on the microscopic capillary effects on higher-order scanning paths, which has not been done so far to our knowledge.
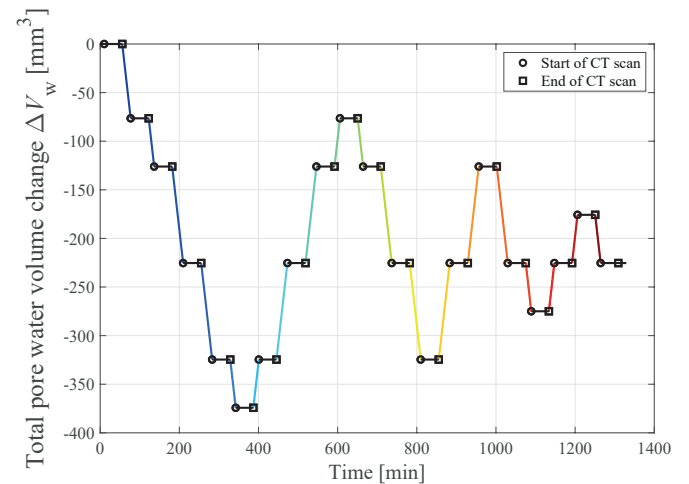

Figure 5. Macroscopic change of pore water volume, applied by the syringe pump, *vs.* time during the hydraulic CT experiment on Hamburg Sand.

In all hydraulic steps, the same flow rate, also chosen in previous experiments [Milatz, 2020], of $\frac{\partial V_w}{\partial t} = 0.0597 \frac{\text{mm}^3}{\text{s}}$, corresponding to $\frac{\partial S_r}{\partial t} \approx 0.000112 \frac{1}{\text{s}}$, has been applied by the syringe pump. This flow rate was shown to be small enough to lead to transient WRCs very close to WRCs measured under equilibrium conditions [Milatz, 2020].

According to the macroscopic assumption of an initially water saturated specimen, the macroscopic degree of saturation is directly calculated from the pore water volume change in the specimen applied by the syringe pump. With the suction response, measured by the integrated pore

Open Geomechanics, 2022, article no. 5
Marius Milatz, Edward Andò, Gioacchino Viggiani & Serge Mora, *In situ X-ray CT imaging of transient water retention experiments with cyclic drainage and imbibition*

6

water pressure sensor underneath a filter plate system in the bottom of the sand specimen, transient WRCs can be reconstructed by combination of applied saturation and measured matric suction. In order to capture the hydraulic behaviour during tomography steps in which no water inflow or outflow could take place, matric suction was measured with a reduced sample rate.

Every CT scan was performed with the same scan-settings, summarised in Tab. 3. In order not to disturb the specimen, the rotational acceleration and deceleration of the rotation stage upon the start and ending of a CT scan was damped using the X-Act software that controls the scanning procedure.

Table 3. Settings of the CT scans at Laboratoire 3SR

X-ray tube voltage	120 kV
X-ray tube current	83 μA
Projections/360° revolution	1120
Isotropic voxel size	10 μm
Binning	1
Averaging	4
Acquisition time per scan	$\approx$ 40 min
Acquisition mode	Continuous rotation

2.5. Evaluation of CT data

Preprocessing

After reconstruction of the CT data, using the filtered backprojection algorithm, built in the X-Act software that also controls the CT scanner at UGA, a stack of 16 bit greyscale tiff-images is obtained. These images include the whole cylindrical sand specimen, including the walls of the acrylic flow cell as well as parts of the topcap and filter stone below the sand specimen. In a first step, the images are cropped by a central circular mask, only selecting the soil volume by blackening the exterior regions using the open-source software FiJi (ImageJ) [FiJi, 2022].

In the further image processing workflow, these images are first filtered using a median filter and a GPU-accelerated non-local means filter based on Gastal and Oliveira [2012], both available in the commercial software Avizo [Avizo 2019.3, 2019]. The combination of these filters allows to reduce noise and to enhance contrast of the different phases sand, water, and air for the following segmentation without a blurring of phase boundaries such as grain edges.

Segmentation

In order to segment or trinarise the image data into the three phases sand, water, and air, a step-wise semi-automatic approach implemented in Avizo is adopted. The 2D-Histogram Segmentation module, following in its implementation the work by Jones et al. [2007], allows to segment different phases with the help of a marker-based water shed algorithm. Individual phases are in a first step detected and pre-labelled (seeded) by means of a 2D histogram plot of their greyscale gradient magnitude *vs.* intensity. Individual

regions are selected based on domains with the highest greyscale gradient magnitude in the 2D histogram by the user. Starting from the pre-labelled regions, a watershed algorithm is applied until all image regions are assigned to an individual material phase. This segmentation procedure helps to reduce the so-called partial volume effect, occurring for standard threshold-based segmentation, that would lead to ill-segmented pixels at phase boundaries, *e. g.*, to the wrong appearance of thin water layers around soil particles. The image processing procedure is illustrated in Fig. 6.
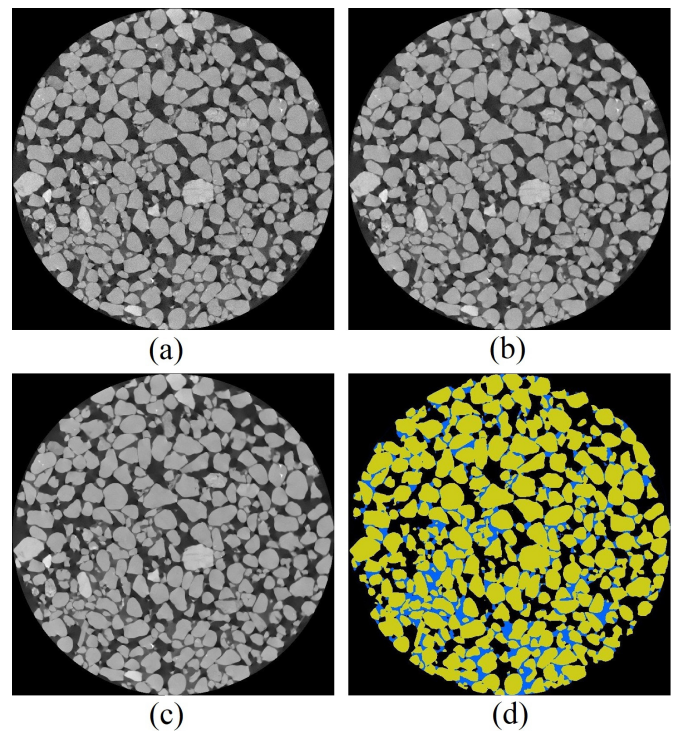

(a)   (b)

(c)   (d)

Figure 6. Image processing procedure including filtering and segmentation: (a) Raw greyscale image, (b) after median filtering, (c) after non-local means filtering, (d) different phases after segmentation.

Analysis of multiphase data and capillary state variables

Different subvolumes are extracted from the whole reconstructed cylindrical specimen volume for the further multiphase analysis of microscopic capillary effects: For the analysis of microscopic phase distribution *vs.* specimen height a central subvolume of 800 px × 800 px × 1145 px (8 mm × 8 mm × 11.45 mm) and for the calculation of averaged unsaturated soil state variables and interfacial properties as well as discontinuous air and water cluster analysis, a cubic subvolume of 800 px × 800 px × 800 px (8 mm × 8 mm × 8 mm) has been selected. Both subvolumes are illustrated in Fig. 7.

With the help of the subvolumes, the evolution of local microscopic averaged properties, such as degree of water and air saturation S_r and S_a, water content w, and void ratio e, can be calculated from the segmented voxel data per slice, *i. e.*, *vs.* specimen height, or within a subvolume. This allows
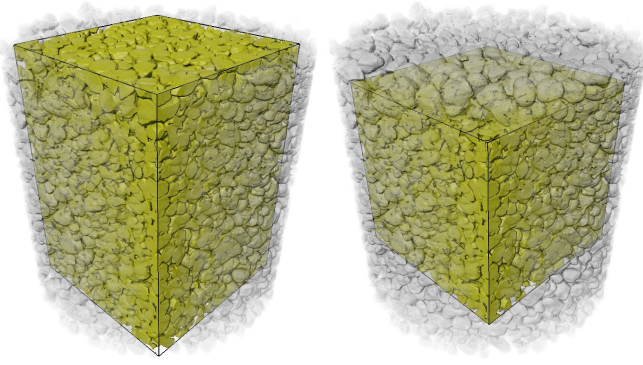
Figure 7. Embedded subvolumes for further analysis of CT data shown within the sand grain skeleton. Left: Subvolume of 800 px × 800 px × 1145 px. Right: Subvolume of 800 px × 800 px × 800 px.

to investigate the evolution of these properties in comparison to their macroscopic values during different hydraulic steps. Fig. 8 shows the location of the discussed subvolumes inside a segmented central vertical slice together with the voxel count of the different phases *vs.* specimen height. From the phase distribution boundary effects can be noticed especially for the air and water phase at the specimen bottom and top. The central cubic subvolume of 800 px × 800 px × 800 px has been selected in a location free of boundary effects representing the bulk of the specimen also excluding the lateral boundaries close to the walls of the flow cell.

The slice-wise microscopic data of void ratio e and water degree of saturation S_r are calculated according to equations 5 and 6. The air degree of saturation can be calculated by $S_a = 1 - S_r$.

$$e = \frac{n_{\text{voxels,a}} + n_{\text{voxels,w}}}{n_{\text{voxels,s}}} \tag{5}$$

$$S_r = \frac{n_{\text{voxels,w}}}{n_{\text{voxels,a}} + n_{\text{voxels,w}}}, \tag{6}$$

where n_{voxels} represents the voxel count per subvolume of the different phases a = air, w = water, and s = solid.

With the help of *labelling*, the air and water clusters inside the experimental data (the central cubic subvolume of 800 × 800 × 800 px is evaluated) can be separated in order to analyse their behaviour with regard to macroscopic degree of saturation and suction during different hydraulic steps. The labelling is computed in Avizo based on connectivity. An individual cluster is defined as the assembly of connected voxels sharing at least one common vertex (voxel corner node) with their neighbouring voxels. We apply a simple counting of individual air and water clusters, an analysis based on cluster volume distribution as well as shape distribution. For the latter, we focus on air clusters which are characterised by Wadell's sphericity ψ [Wadell, 1935] calculated for their volume V and surface area A according to Eq. 7. Wadell's sphericity represents the relationship of the surface area of a sphere with the same volume as the considered particle to its true surface area, yielding $\psi = 1$ if the considered particle is a perfect sphere itself and values which are the lower the more the considered particle

deviates from a sphere.

$$\psi = \frac{\pi^{\frac{1}{3}}(6V)^{\frac{2}{3}}}{A} \tag{7}$$

As transient hydraulic drainage and imbibition paths are followed during the experiment, also the evolution of the nonwetting-wetting fluid interfacial area (air-water interfacial area) a^{nw} and the solid-wetting fluid interfacial area (solid-water interfacial area) a^{sw} per unit volume are calculated for every hydraulic step. For this purpose, the interfaces of different phases are detected and approximated by a triangulated surface mesh using the Avizo software. In Avizo, the selected settings for the control of the surface meshes include (1) an option to optimise or compact (Avizo-terminology: "compactify") the extracted meshes in a post-processing approach, (2) the option to adjust coordinates to lie exactly on the nearest boundary face of the bounding box including the surface, and (3) a constrained smoothing procedure, ensuring thin regions not to vanish at the lowest possible smoothing extent. The presented interfacial areas have been computed with these optimal settings yielding the highest possible accuracy. As compared to a surface generation with the default settings without "compactifying" the mesh and with a medium constrained smoothing extent, the selected settings at the highest possible accuracy of surface approximation resulted in an average increase of *ca.* 25 % of the air-water interfacial area and of *ca.* 9 % of the solid-water interfacial area, which probably accounts for fine surface structures being missed or smoothed out when the default meshing settings are used. It should be the task of future studies to further assess the accuracy and also the effect of different input voxel sizes on the accuracy of interfacial area measurements based on this methodology.

The solid- and air-water interfacial areas have been measured based on the available phase segmentation relying on the image resolution at a voxel size of 10 μm. It must be noted that potential thin liquid layers on the solid grain surfaces as a basis for film flow as discussed in some studies, *e. g.*, Tuller et al. [1999] and Tuller and Or [2001], can't be resolved at this resolution and therefore are not considered in the determination of the interfacial areas.

A further geometric measure of capillary action is the contact line representing the location shared by all present phases where interfacial tension is transferred to the solid grains. It is measured in the central cubic subvolume as a 3D path, consisting of nodes and line segments, the length of which can be measured to calculate the specific length of the contact line per unit volume. For the determination of contact line, the 3D intersections of all phase surfaces are detected in Avizo using the "Create Surface Geodesic Path" module applied to a surface mesh of all materials inside a subvolume. The surface contours, representing the common 3D line of all phases, including background, are imported, split at intersections to create many nodes, linked by segments, transformed into a spatial graph, and finally filtered by bounding box contact to remove the segments touching the exterior material, *i. e.*, the bounding box. This procedure yields the 3D contact line, touching all phases as
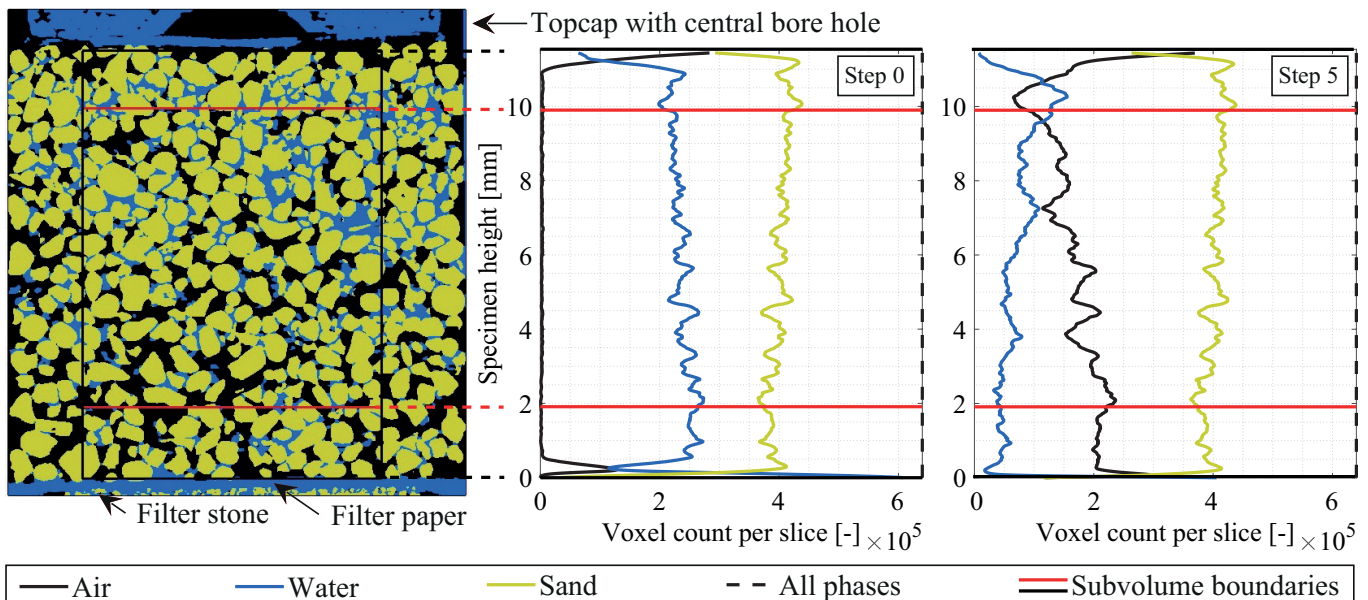
Open Geomechanics, 2022, article no. 5
Marius Milatz, Edward Andò, Gioacchino Viggiani & Serge Mora, *In situ X-ray CT imaging of transient water retention experiments with cyclic drainage and imbibition*

8

Figure 8. Location of subvolumes marked in a central vertical slice of segmented CT data for step 5 of the hydraulic experiment on Hamburg Sand and phase-specific voxel count for step 0 and step 5. Black boundary: Subvolume of 800 px × 800 px × 1145 px. Red boundary: Subvolume of 800 px × 800 px × 800 px.

illustrated in Fig. 9 for the experimental step with the lowest degree of saturation after primary drainage. More detailed visualisations of the contact line are given in Fig. 29 in the Appendix section.

As a further analysis of microscopic properties, the shape of different selected menisci in the pore space can be characterised by their contact angles θ to adjacent grains as well as their radius of curvature in order to investigate the phenomenon of contact angle-hysteresis as well as capillary pressure on the grain scale. By tracing the interface between air and water, different menisci are identified in various 2D slices in x-, y- and z-direction of the 4D data set, allowing to manually measure contact angles and radii of curvature for all hydraulic steps. Contact angles are measured using the contact angle tool in the open-source software Fiji (ImageJ). The same software is used to measure radii of curvature by fitting a circle to the curvature of the considered meniscus if possible. This proposed method is limited by the available image resolution (in this case 0.01 mm/px) and by image noise. For an improvement of the quality of measurements, the evaluation is based on greyscale images, filtered greyscale images and Sobel filtered greyscale images, the last of which enhance the edges of grains and menisci. The procedure is illustrated in Fig. 30 in the Appendix.

In order to obtain reliable results, a multitude of measurements is taken on selected menisci in all space directions, resulting in a point cloud of ideally two contact angles and one radius of curvature for each considered meniscus. For further analysis, the measured radius of curvature R_1 allows to calculate mean curvature H and capillary pressure p_c according to Eq. 4 under the assumption that the second radius of curvature R_2 is infinity under 2D conditions. The contribution of the second (perpendicular) radius of curvature to mean curvature is neglected. The calculated capillary

pressure is then compared to the measured matric suction to link the microscopic and macroscopic scale.

Analysis of grain kinematics and pore-saturation

The discrete digitial image correlation (DDIC) algorithm, implemented in the open-source software spam [Stamati et al., 2020], has been used to track grain displacements in 3D data sets from the first six time steps, including the initial water-saturated specimen state and the consecutive five incremental hydraulic steps during primary drainage. The DDIC analysis works on labelled images, only containing the solid, *i.e.*, the sand phase. The result of a total correlation analysis yields the discrete 3D particle positions over time to investigate grain displacements which are coupled to the drainage process. Furthermore, a pore-based analysis of emptying events has been run based on a radical Delaunay triangulation, linking grain centres to form a mesh of tetrahedral volume elements. The triangulation is calculated for every time step. The voxel count of segmented images on which the triangulation is mapped is used to calculate pore-based statistics, *e.g.*, of a pore-saturation, during the drainage process. In this approach, a pore is defined as the volume of a tetrahedron minus the volume of the solid phase contained in the tetrahedron. Pore-saturation can thus be calculated as the water volume per pore volume for every pore inside one of the many tetrahedra. Note that the characterisation of pores by tetrahedral elements linking the grain centres represents a discrete approximation which might capture a "regular pore", *i.e.*, a pore in between only four neighbouring grains, better than a pore enclosed by a multitude of neighbouring grains. In the latter case, the pore will be represented by more than one tetrahedral element, *i.e.*, it will be discretised. Further future studies should evaluate and quantify the accuracy of the approach for different
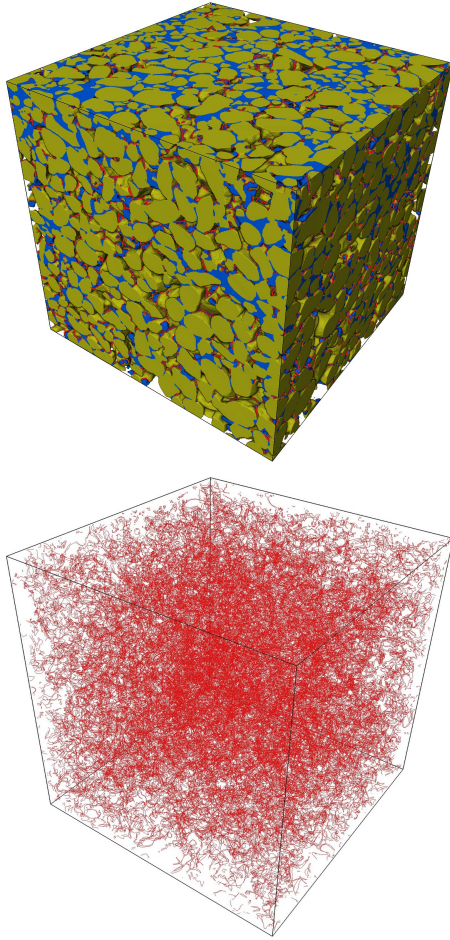
Figure 9. Visualisation of the 3D contact line in a cubic subvolume containing Hamburg Sand and water at the lowest degree of saturation after primary drainage with the contact lines highlighted in red colour (top) and extracted 3D contact line (bottom).

granular materials, *e. g.*, ideal sphere packings compared to arbitrarily shaped grains.

3. Experimental results

3.1. Macroscopic water retention behaviour

The time-histories of applied change in macroscopic degree of saturation and the measured suction response are shown in Fig. 10. Test stages, such as tomography steps, in which data was logged without a change in macroscopic specimen water content, are indicated in black colour. Each of the 19 hydraulic test stages is plotted in a different colour.

A clear response of matric suction upon change of degree of saturation can be noticed from the data time-histories. Especially upon primary drainage, heavy oscillations and jumps of matric suction upon air entry into the specimen are measured. During the first CT scan, an increase in matric suction can be noticed which might be due to the effect of the specimen topcap having been pushed on top of the specimen directly prior to the scan. The oscillations on the primary drainage path typically occur when air enters the
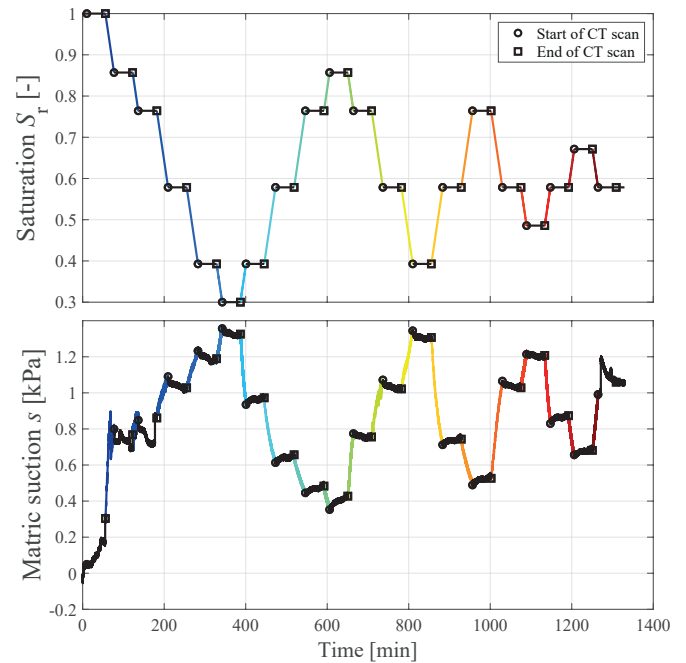

Figure 10. Macroscopic change of degree of saturation calculated from the pore water volume change (top) and measured suction response (bottom) *vs.* time during the hydraulic CT experiment on Hamburg Sand.

specimen top and breaks through onto the filter system at the base of the specimen. This behaviour could be well observed through the acrylic cell during experiments under lab conditions presented in Milatz [2020]. The analysis of phase distribution by means of X-ray CT will make it possible to further elevate these simple observations from the specimen's exterior into the 3D void space inside the specimen.

During image acquisition, when no macroscopic flow of pore water into or out of the specimen is applied, a characteristic drift or relaxation of matric suction can be observed which might indicate a transient redistribution of pore water inside the specimen after the pore water flow is stopped. Another explanation could be a slight impedance of pore water flow caused by the applied membrane and porous stone filter. After the termination of a drainage step, matric suction always slightly decreases before stabilising on a plateau, while matric suction always increases after the end of an imbibition step. This relaxation of matric suction can be observed to be within a limiting magnitude of ca. ∓0.06 kPa in nearly all cases.

The macroscopic WRC, obtained by combination of the data presented in Fig. 10, is shown in Fig. 11. The transient water retention data is also compared to the primary drainage path measured with the HYPROP evaporation test [Peters and Durner, 2008, UMS, 2018] on the same sand at the same initial macroscopic void ratio. The slopes of the primary paths measured in the transient experiment and the HYPROP test are in good agreement. However, deviations due to the effect of suction oscillations at air entry occur on the primary drainage path. The measured step-wise

drainage and imbibition scanning paths can be assembled to a WRC with the typical ellipsoid hydraulic loops with the scanning paths approaching the primary drainage and main imbibition paths asymptotically. The aforementioned relaxation effects are also visible in the s-S_r-space.
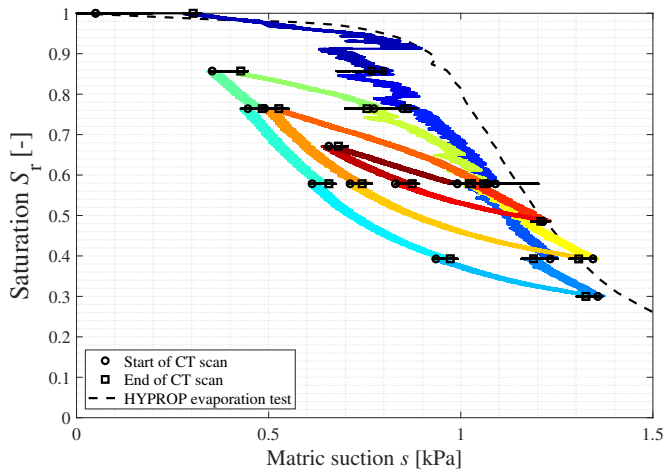

Figure 11. Macroscopic transient water retention curve with intermediate tomography steps measured during the hydraulic CT experiment on Hamburg Sand.

The transient WRC measured here is very similar to the WRCs measured for the same material at the same macroscopic initial void ratio under lab conditions presented in Milatz [2020]. In contrast to the WRCs measured continuously without intermediate tomography steps, the suction range between highest and lowest suction of the hysteresis loops is narrower which might be due to the inward relaxation of matric suction occurring in the transient CT experiment.

3.2. Multiphase analysis of microscopic properties

Evolution of subvolume-based specimen properties

Fig. 12 shows the changing distribution of pore water in a reconstructed subvolume of 800 px × 800 px × 1145 px consisting of the solid sand phase and water phase for the initial specimen state and the successive 19 hydraulic steps in the hydraulic experiment on Hamburg Sand. The same experimental steps are shown for the air phase only in Fig. 13. Especially in the five initial images, a developing vertical and then branching air channel, reaching from specimen top to the bottom, can be noticed. A time series of the water phase only is illustrated in Fig. 31 in the Appendix.

The local distributions of void ratio e, water degree of saturation S_r, and air degree of saturation S_a inside the central subvolume of 800 px × 800 px × 800 px edge length are shown in Fig. 14 vs. specimen height for all hydraulic steps. The hydraulic steps after which the CT data have been obtained are indicated by a heat map with cold blue colours

representing the initial steps and dark red colours indicating the final steps of the hydraulic experiment. This visualisation allows to evaluate the phase homogeneity as well as boundary effects especially at the specimen top where the air enters the specimen and at the bottom where the water flow boundary condition is applied.

It can be seen that the void ratio is limited by the minimum and maximum values $e_{\min}$ and $e_{\max}$ as given in Tab. 1. The mean void ratio, calculated from the slice-wise voxel-based data, is lower than the macroscopic void ratio of $e_0 = 0.65$ aimed for in specimen preparation. From the void ratio distribution a higher densification of the specimen at the top of the considered subvolume can be noticed. During the hydraulic cycles, a very small change in void ratio seems to occur, with the void ratio slightly increasing at the specimen bottom and decreasing at the specimen top if the experimental steps 0 and 19 are compared. This observation might be an evidence for microscopic hydro-mechanical coupling effects due to which grain movements develop during cyclic pumping of pore water or reordering of capillary bridges and water clusters.

The distributions of S_r and S_a indicate a nearly full water saturation with an average of $S_r = 0.988$ in the considered subvolume at the beginning of the experiment (step 0). Accordingly, the amount of entrapped air initially equals an average of $S_a = 0.012$. In the first two hydraulic steps, a reduction of degree of saturation or an increase in air degree of saturation starting from the specimen top, but also strongly propagating close to the bottom of the considered subvolume can be noticed. Focusing on the air distribution, this behaviour corresponds well to the sudden break through of an air channel from specimen top to bottom that further branches laterally to the sides in the lower zone of the pore volume during primary drainage, which has already been observed in the reconstructed image sequences shown in Fig. 12 and Fig. 13 for the step in between $S_r = 0.86$ and $S_r = 0.76$. As larger voids are emptied before smaller voids at the same capillary pressure, a vertical air channel could rapidly break through the specimen at primary drainage and reach out horizontally around the bottom regions of the specimen. This sudden air distribution also represents an explanation for the suction drop measured macroscopically around air entry shortly before the third CT scan after the second hydraulic drainage step as shown in Fig. 11. The air clusters close to the filter system below the specimen shortly cut off the hydraulic contact to the pore pressure sensor in the drainage system. Therefore, temporarily no good suction response is measured until hydraulic contact is reestablished on further drainage or imbibition with water redistribution.

After the third hydraulic step, also the middle parts of the subvolume are filled with pore air, leading to a more homogeneous distribution of S_r and S_a vs. specimen height. However, a gradient within the air and water distributions develops during all consecutive drainage and imbibition steps, with more air being entrapped in lower parts closer to the specimen bottom. Accordingly, more pore water remains in the upper part of the specimen. This finding correlates well with the smaller void ratio in this region of the specimen,
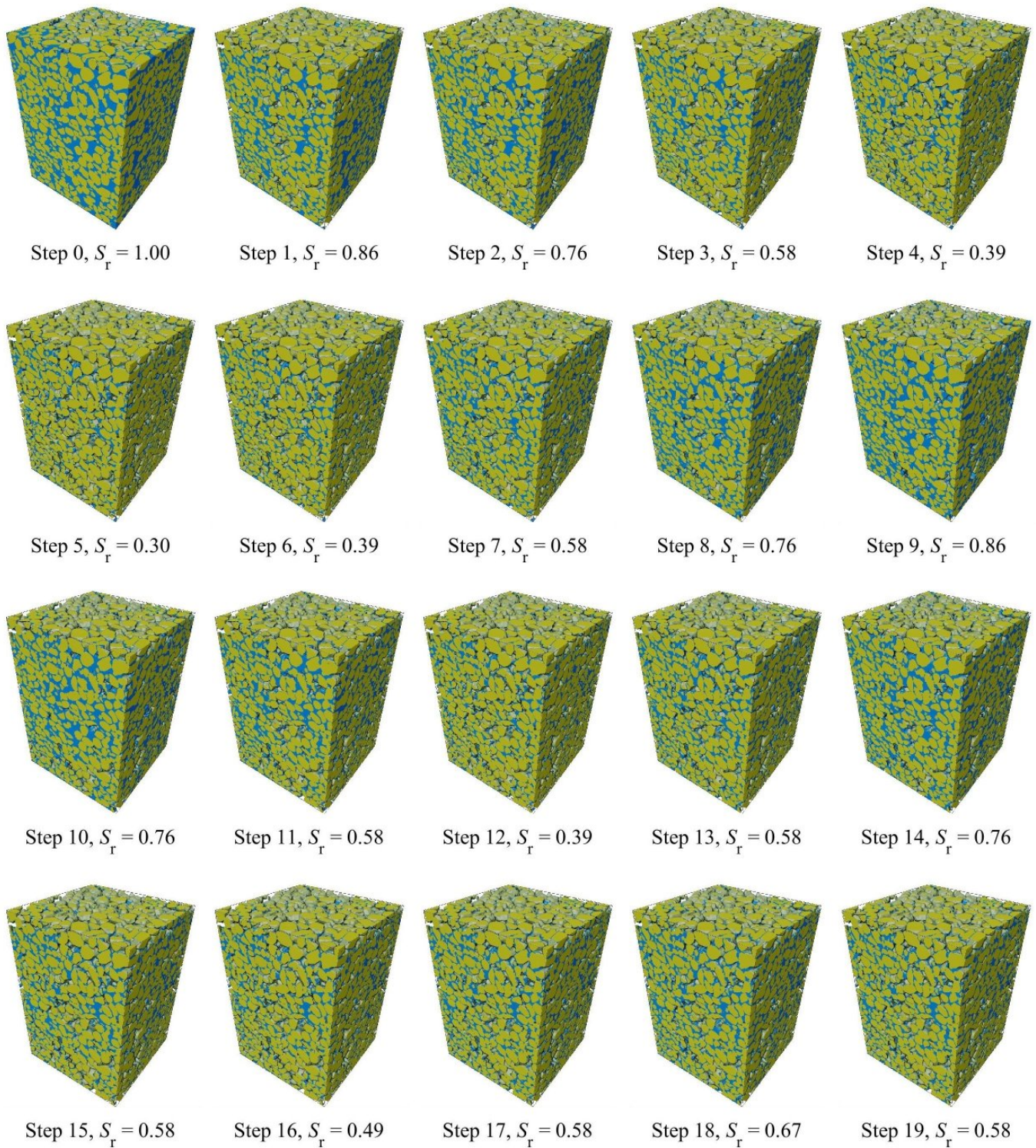
Open Geomechanics, 2022, article no. 5
Marius Milatz, Edward Andò, Gioacchino Viggiani & Serge Mora, *In situ X-ray CT imaging of transient water retention experiments with cyclic drainage and imbibition*

11

Figure 12. Cyclic drainage and imbibition on a subvolume of 800 px × 800 px × 1145 px (8 mm × 8 mm × 11.45 mm). Reconstructed sand (yellow) and water volumes (blue). Air volumes are not shown. Step 0 indicates the water-saturated initial specimen state. Hydraulic steps and macroscopic degree of saturation according to Fig. 10.

where a higher capillary pressure retains the pore water with more strength compared to regions with higher void ratio according to the rules of capillarity.

By means of averaging of phase-specific voxel data over a subvolume, local soil state variables, such as void ratio and degree of saturation, can be calculated directly from the image data and compared to the macroscopic variables as prescribed in the experiment. The evolution of S_r and e, calculated for the central cubic subvolume of 800 px × 800 px × 800 px, *vs.* experimental steps is shown in Fig. 15.
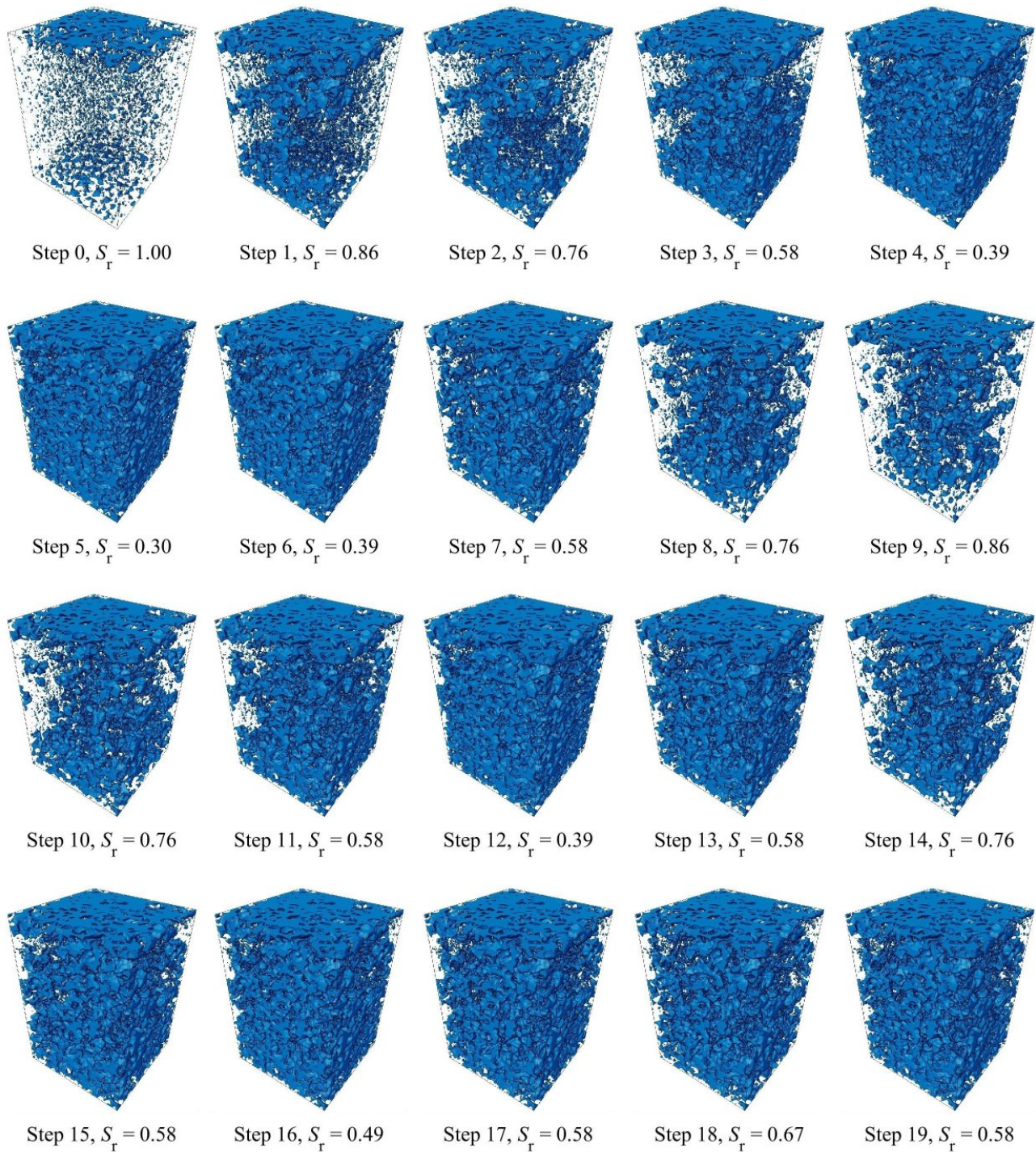
Figure 13. Cyclic drainage and imbibition on a subvolume of 800 px × 800 px × 1145 px (8 mm × 8 mm × 11.45 mm). Reconstructed air volumes (blue). Step 0 indicates the water-saturated initial specimen state, where occluded air bubbles and larger air clusters at the specimen top can be found. Hydraulic steps and macroscopic degree of saturation according to Fig. 10.

The comparison of macroscopic and local (subvolume-based) degree of saturation generally shows a good agreement. Especially for the end of primary drainage, for the following main imbibition and for the first scanning drainage path, a good agreement of macroscopic and local data derived from the voxel distribution inside the subvolume can be noticed. During primary drainage and in the last three

scanning paths starting with step 14, higher deviations occur. These deviations might be due to local inhomogeneities in the pore water distribution as well as boundary effects at the specimen top and bottom or at the cylindrical side walls
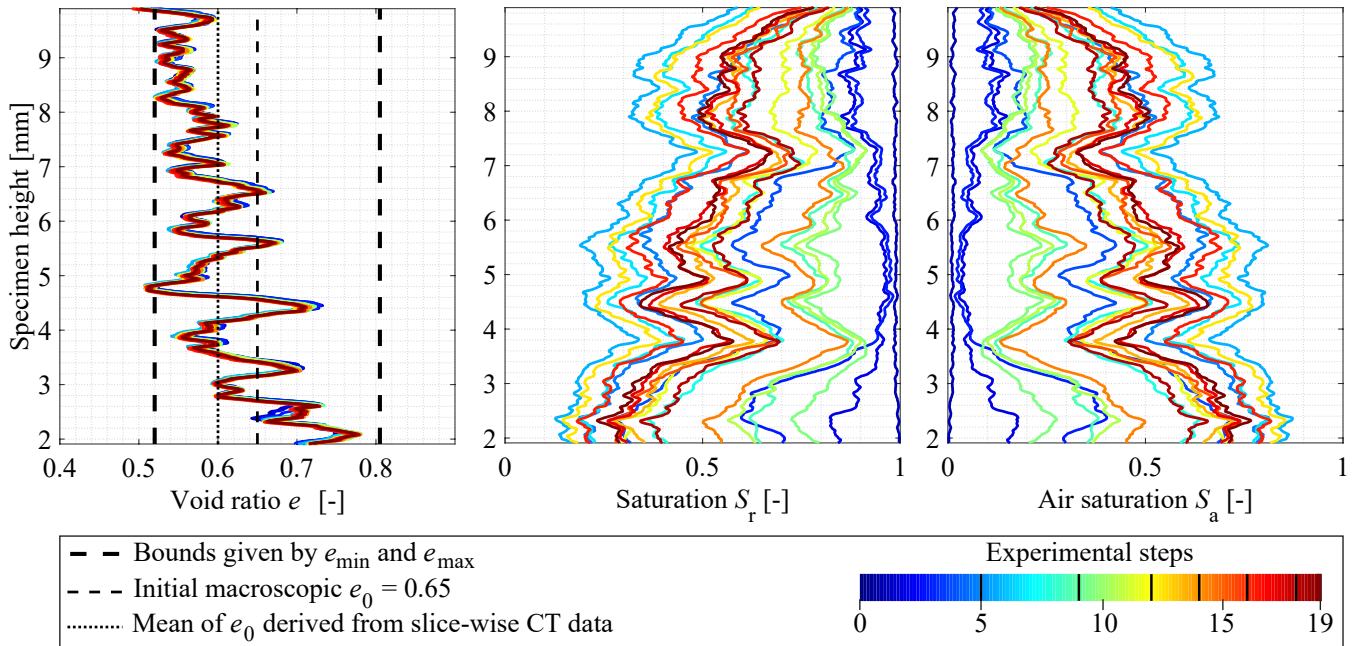
Figure 14. Evolution of soil properties e, S_r, and S_a *vs.* specimen height from a central cubic subvolume of 800 px × 800 px × 800 px during the hydraulic CT experiment on Hamburg Sand. Experimental steps after which a change in flow direction takes place are indicated by a black bar in the colourbar.
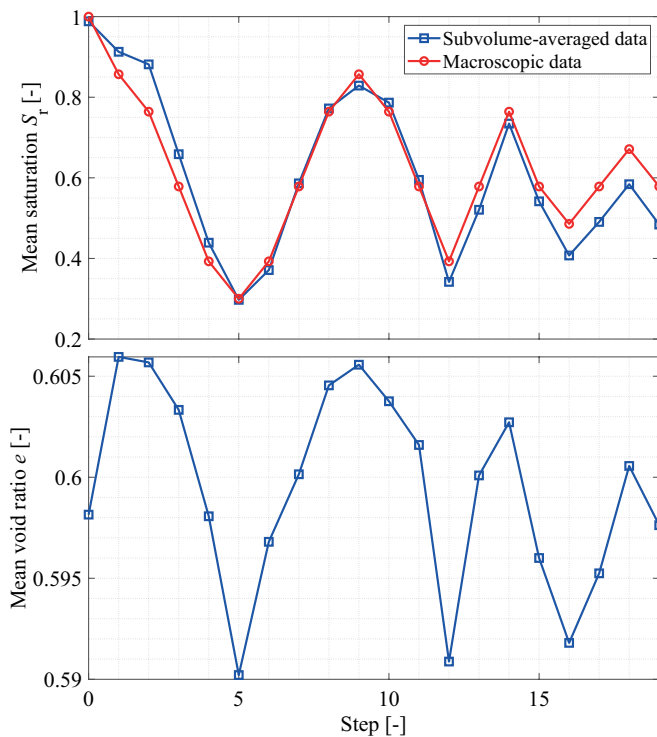

Figure 15. Evolution of prescribed macroscopic degree of saturation and calculated subvolume-based (averaged) local degree of saturation (top) as well as change of calculated subvolume-based (averaged) local void ratio (bottom) for all hydraulic steps in the CT experiment on Hamburg Sand.

of the specimen container which are not affecting the selected cubic subvolume. Furthermore, the macroscopic degree of saturation is calculated based on the initial macroscopic specimen volume and according to pore water volume change applied by the syringe pump, without taking microscopic air entrapment, evaporation as well as phase inhomogeneities into account.

The evolution of void ratio in Fig. 15 reveals a cyclic "breathing" of the pore volume, closely coupled to the change in degree of saturation, which might represent direct evidence for the hydro-mechanical coupling and the volumetric impact of changes in suction stress in granular media. If the sudden increase of void ratio due to the first hydraulic step is neglected, a clear reduction of void ratio upon drainage and an increase upon imbibition can be derived from the data. Furthermore, the magnitude of void ratio change seems to be directly coupled to the magnitude of change of degree of saturation. This characteristic behaviour is also underlined when the void ratio is plotted *vs.* degree of saturation or matric suction as in Fig. 16. Void ratio data are shown *vs.* matric suction before and after a CT scan. An increase in matric suction corresponds to a volumetric contraction of the grain skeleton and pore volume, whereas a decreasing suction leads to relaxation and dilation.

Water and air cluster analysis

The evolution of the air and water cluster count *vs.* degree of saturation and matric suction of all hydraulic steps is shown in Fig. 17.

Interestingly, both air and water cluster counts show hysteresis when plotted *vs.* matric suction and degree of saturation. However, the hysteresis is more pronounced when
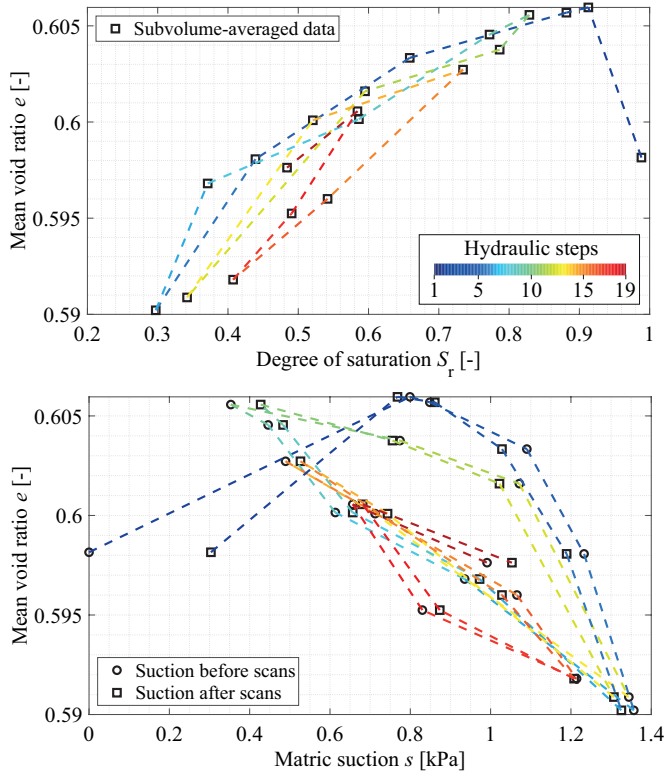
Figure 16. Evolution of subvolume-based (averaged) local void ratio *vs.* subvolume-based local degree of saturation (top) as well as *vs.* measured macroscopic matric suction before and after a tomography step (bottom) for all hydraulic steps in the CT experiment.

the cluster counts are shown *vs.* matric suction (compare right to left column of Fig. 17). Especially the air cluster count seems to show some drift when shown *vs.* degree of saturation, which might be a consequence of air entrapment during different hydraulic cycles. The maximum number of air clusters contained in the considered subvolume is higher than the number of water clusters, which can be explained by water, being the wetting phase, rather forming connected clusters than isolated volumes which is a characteristic of air as the nonwetting phase.

Further 3D histograms showing the evolution of water and air clusters in 10 different volume domains for all hydraulic steps are shown in Fig. 32 and Fig. 33 in the Appendix. Especially for air clusters, but also for water clusters, very small volumes dominate all present clusters, which might also be due to image noise. During the hydraulic cycles and individual steps, clusters of different volumes appear and disappear at different times. The effect of changing water drainage and imbibition steps is especially visible in the histogram for the water clusters, with the number of clusters increasing and decreasing in different volume domains, whereas especially smaller air clusters don't seem to be much influenced by changing water flow directions. This might be evidence for the entrapment of especially smaller air volumes in the pores.

In the air bubble shape analysis, labelled air volumes are classified by their sphericity ψ. We firstly analyse the

evolution of the number of air clusters for ten sphericity domains as shown in Fig. 18. A visualisation of the considered sphericity ranges is shown in Fig. 34 in the Appendix. The closer ψ is to one, the closer the corresponding air cluster is to a spherical volume, *i.e.*, a bubble. The lower ψ, the more the corresponding air cluster resembles a volume with complex shape, such as air ganglia. From Fig. 18 it can be seen that air clusters with $\psi \geqslant 0.50$ dominate the air volumes present in the considered subvolume. While rather less spherical ganglia with $0.70 < \psi \leqslant 0.80$ represent the maximum number of air clusters present during all hydraulic steps, the initially very present spherical bubble-like air volumes of the shape group $0.90 < \psi \leqslant 1.00$ are much reduced during primary drainage and consecutive drainage steps, without being much renewed during imbibition steps. However, also close to spherical air bubbles of the shape group $0.80 < \psi \leqslant 0.90$ seem to stabilise in the pores. By analysing the relationship between air cluster volume and air cluster sphericity (not shown here), it can be shown that increasing sphericity relates well to smaller volumes.

The data presented in Fig. 19 show the trends of the minimum, mean, and maximum value of sphericity ψ for all air clusters present after all hydraulic steps. As already could be inferred from the data in Fig. 18, the decrease in maximum and mean sphericity with increasing number of hydraulic cycles indicates that the air clusters more and more take the forms of complex ganglia, whereas smaller rather spherical clusters are reduced. These results illustrate that hydraulic hysteresis is, amongst other physical phenomena, such as contact angle hysteresis, obviously related to air and water phase distribution and shape (morphology) which both change during different drainage and imbibition cycles.

Evolution of interfacial areas

As recent mathematical approaches for the evaluation of effective stress in unsaturated soils include the effect of the microscopic interfaces, *e.g.*, Gray et al. [2009], Lu et al. [2010], Nikooee et al. [2013], and Wang et al. [2019], and also macroscopic hysteresis of the WRC is believed to be linked to them, *e.g.*, Hassanizadeh and Gray [1990], the evolution of the interfacial areas a^{nw} and a^{sw} is of interest. Both soil properties have been extracted as subvolume-averaged data from the selected central cubic subvolume of 800 px × 800 px × 800 px for all hydraulic steps of the experiment.

When the interfacial areas are plotted *vs.* the local degree of saturation inside the subvolume as well as macroscopic matric suction, characteristic curves of a^{nw} and a^{sw} are obtained in Fig. 20.

While especially the solid-water interfacial area nearly shows no hysteresis, but rather a monotonic curve when plotted *vs.* corresponding degree of saturation, and the air-water interfacial area shows some slight hysteresis or shift (compare left column subplots of Fig. 20 a) and b)), both interfacial area properties are highly hysteretic when plotted *vs.* macroscopic matric suction, reproducing elliptical loops as known from the WRC (compare right column subplots of Fig. 20 c) and d)). Especially the solid-water interfacial area seems to be directly linked to degree of saturation due to the monotonic slope, when shown *vs.* saturation and due to the
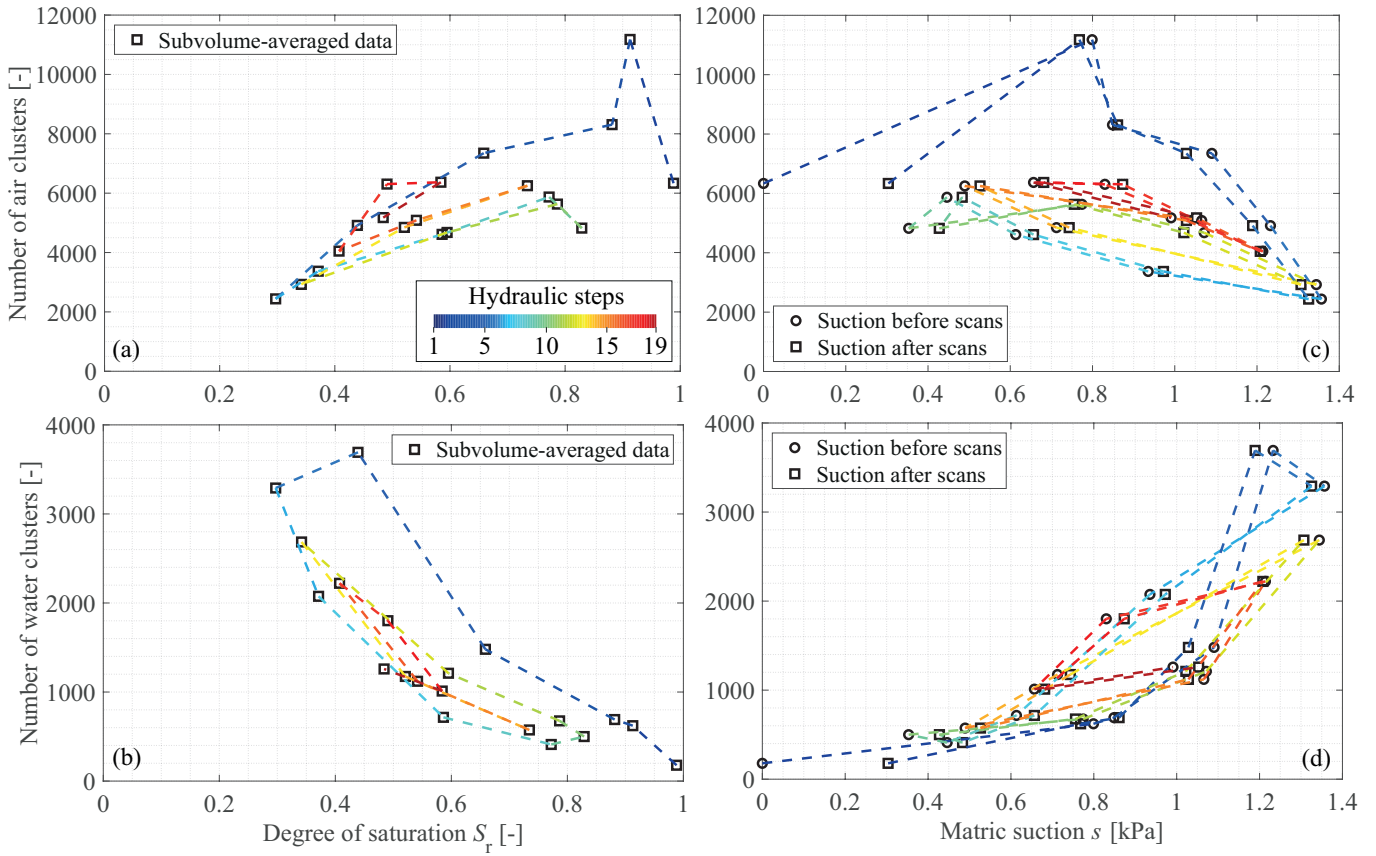
Figure 17. Evolution of (a) air cluster count, (b) water cluster count *vs.* degree of saturation, (c) air cluster count and (d) water cluster count *vs.* matric suction for all hydraulic steps.
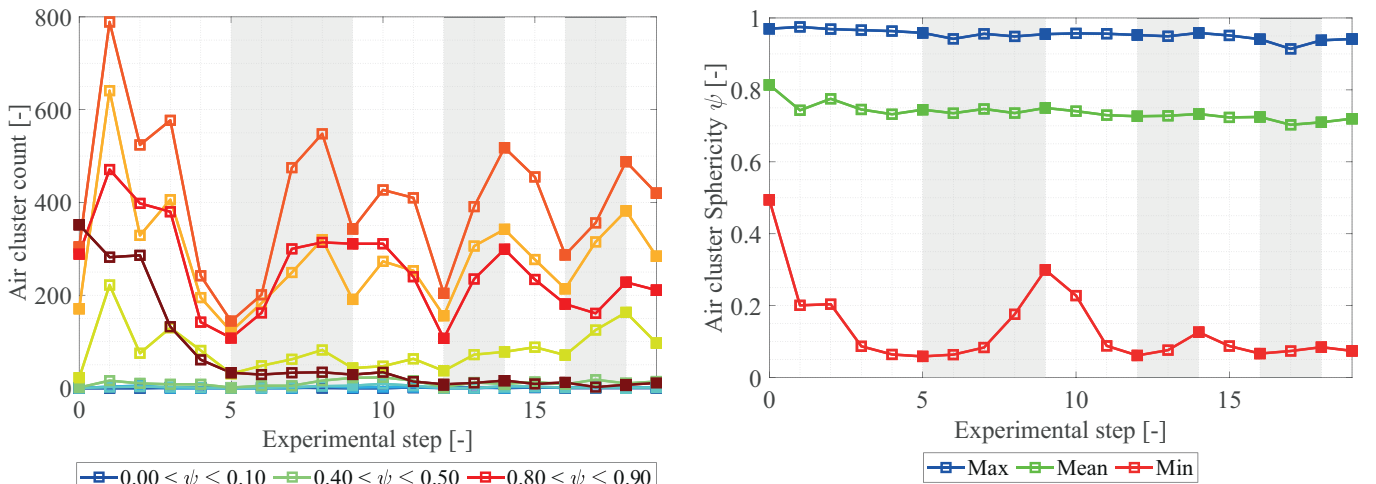

Figure 18. Evolution of air cluster count in different sphericity groups contained in the cubic subvolume for all hydraulic steps. Imbibition steps are highlighted by a grey background.
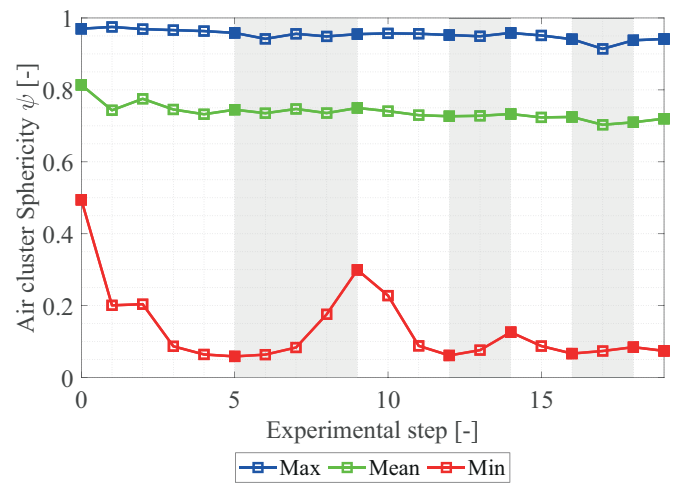

Figure 19. Evolution of maximum, mean, and minimum sphericity of all air clusters contained in the cubic subvolume for all hydraulic steps. Imbibition steps are highlighted by a grey background.

resemblance of the a^{sw}-s-curve to the WRC. The monotonic a^{sw}-S_r-curve appears to be limited by $a^{sw} = 0$ for $S_r = 0$ and $a^{sw} = a^s$ for $S_r = 1$, with a^s being the solid surface area per total volume, also known as the specific surface area of the granular material. For $S_r = 1$, the solid-water interfacial area approaches a value of $a^{sw} \approx 6.2$ mm^2/mm^3 which is very close to the value of $a^s = 6.28$ mm^2/mm^3 as measured from CT data of grain surface contained in the considered subvolume. This being said, a^{sw} becomes a concrete measure of
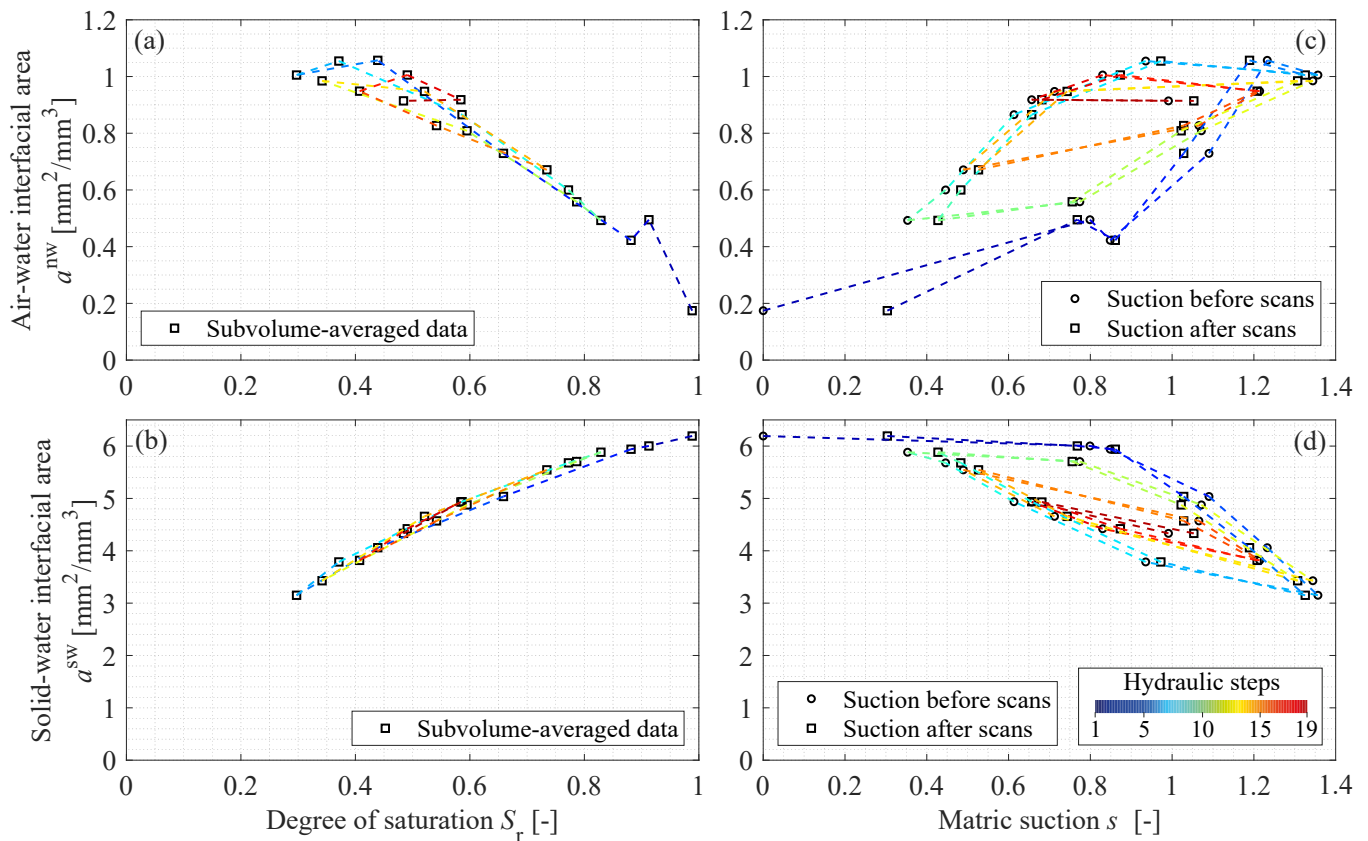
Figure 20. Evolution of (a) air-water interfacial area, (b) solid-water interfacial area *vs.* degree of saturation, (c) air-water interfacial area, and (d) solid-water interfacial area *vs.* matric suction for all hydraulic steps.

the wetted solid surface, with its magnitude and characteristic possibly depending on the grain size and grain shape distribution. This needs further investigations, especially for other granular materials.

The air-water interfacial area has to be zero for $S_r = 0$ and $S_r = 1$ with a peak value in between. From Fig. 20 a) the peak value can be located around $S_r = 0.4$. Generally, a^{nw} seems to be higher on imbibition paths compared to drainage paths for the same degree of saturation and suction levels as shown in Fig. 20 a) and c). This could be a consequence of contact angle hysteresis. However, the solid-water interfacial area is always higher on drainage paths compared to imbibition paths when shown *vs.* matric suction in Fig. 20 d).

Evolution of specific contact line

The measured specific contact line, representing the reference line for the action of interfacial tension per unit volume, is also studied as a function of degree of saturation and matric suction based on Fig. 21.

Similar to the air-water interfacial area, the specific length of contact line is increasing with decreasing degree of saturation, probably reaching a maximum for some lower degree of saturation and reaching zero in the fully dry state. When plotted *vs.* matric suction, the specific length of contact line also shows pronounced hysteresis, whereas it rather drifts when shown *vs.* degree of saturation. At its maximum measured here, one cubic millimetre of sand

contains nearly 60 mm of curled contact lines oriented in all directions of space. If the contact line is imagined as the measure of length along which interfacial tension acts onto the grains, it can be seen as another quantitative measure for hydro-mechanical coupling in the unsaturated state. Similar to the interfacial areas, also the specific length of contact line together with contact angles could therefore be characteristic of the tested material and act as an ingredient for effective stress or for the construction of a unique relationship for the WRC based on capillary state variables, which is addressed in the following, but which should be further tested in the future.

Meaning of interfacial capillary state variables regarding a unique WRC

If we plot the degree of saturation and air-water interfacial area derived from the extracted subvolume of CT data together with matric suction measured after each CT scan, we can establish a unique relationship in the form of a 3D surface, expressing a^{nw} as a function of S_r and s as shown in Fig. 35 in the Appendix. The function $a^{nw} = f(S_r, s)$, fitted to the 3D data points, is a quartic polynomial surface function, intended only to proof that the data can be fitted well by a 3D surface. On the way to a unique relationship for the WRC based on capillary state variables, this represents evidence for the theoretical considerations of Hassanizadeh and Gray [1990] and Hassanizadeh and Gray [1993], suggesting that our view of the WRC as a functional relationship between S_r
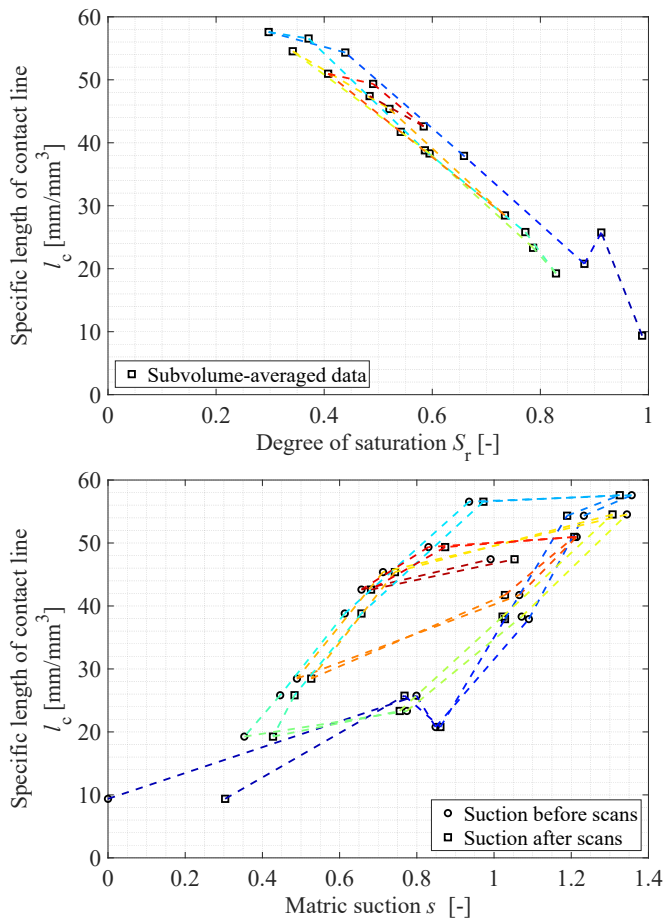
Figure 21. Evolution of specific length of contact line *vs.* degree of saturation (top) and *vs.* matric suction (bottom) for all hydraulic steps.

and s is incomplete. It also confirms the findings by Porter et al. [2009] who also discovered a similar state surface for a glass bead packing.

Although not shown here, similar dependencies and surface approximations can also be found for the solid-water interfacial area and for the specific contact line. This highlights that the capillary state variables are deeply connected to degree of saturation and capillary pressure with the hysteresis phenomenon occurring in a kind of "state surface".

Evolution of individual capillary menisci

The contact angles measured on individual menisci are plotted *vs.* all hydraulic steps in Fig. 22. Due to the time required for CT imaging after a hydraulic step, the contact angles are assumed to be equilibrium contact angles if a potential effect of specimen rotation, evaporation, and viscous effects causing relaxation of the air-water interfaces is neglected.

The development of the mean of the contact angles shows clear evidence for contact angle-hysteresis, with lower mean contact angle on drainage paths compared to imbibition paths. However, the mean contact angle is gradually increasing and decreasing, which underlines that the change in the shape of menisci is a gradual process
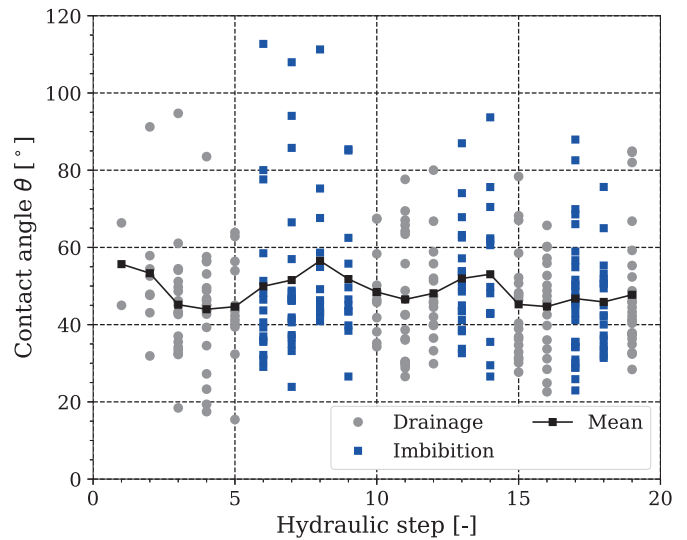

Figure 22. Evolution of measured contact angles for all drainage and imbibition steps.

upon flow reversal. Some of the drainage contact angles are higher compared to imbibition contact angles, which can be explained by pinning of menisci, observed in some images, when menisci adhere to rough grain surfaces or sharp edges in pore throats. The pinning prevents the free movement of the menisci so that their curvature and also the contact angle is forced to change. In rare cases, also convex menisci with a negative radius of curvature could be observed.

A histogram of contact angles on drainage and imbibition paths is presented in Fig. 23. Here, a similar distribution of contact angles on drainage and imbibition paths can be noticed. However, for imbibition, the probability of larger contact angles is higher compared to drainage. Out of 182 drainage contact angles and 141 imbibition contact angles measured, the mean drainage contact angle is 46.478°, whereas the mean imbibition contact angle is calculated as 50.307°, also showing the effect of contact angle-hysteresis.
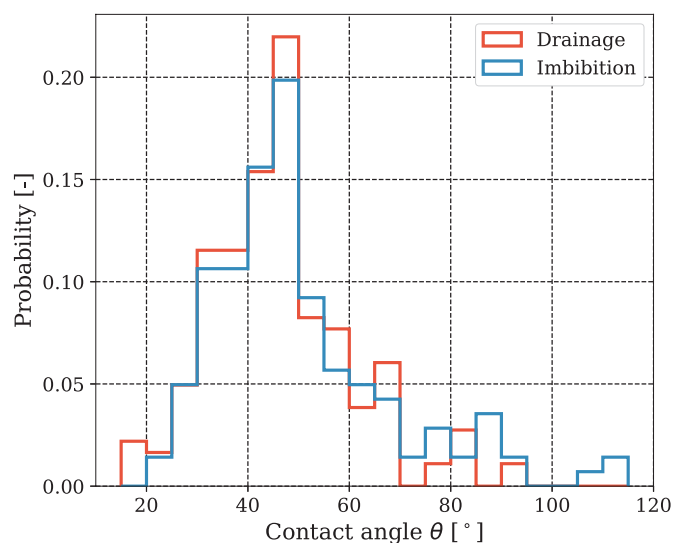

Figure 23. Probability distribution of contact angles measured on drainage and imbibition paths.

Besides the contact angles, the radius of curvature is also closely associated with geometry of a capillary meniscus and will change upon drainage and imbibition if no pinning effects occur. The radius of curvature is especially interesting because it allows to calculate capillary pressure. The evolution of the 2D radii of curvature measured for many menisci during all hydraulic steps is shown in Fig. 24. Similar to the contact angle, the mean of radius of curvature shows hysteresis. Smaller radii of curvature are measured on drainage paths compared to imbibition paths, although there is also a gradual formation of radii of curvature as drainage or imbibition proceed. This underlines the kinematics of single menisci during continuing drainage or imbibition. The hysteresis of matric suction therefore seems to be correlated to different radii of curvature and contact angles on drainage and imbibition paths.
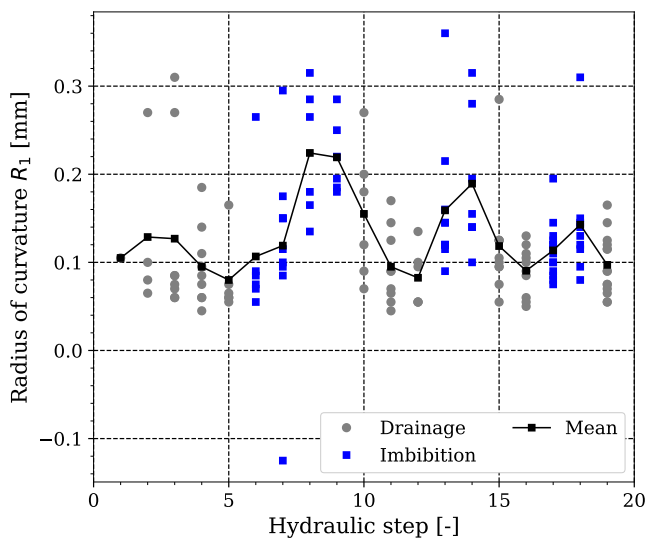

Figure 25. Measured radii of curvature R_1 plotted *vs.* the contact angles θ of the same meniscus with linear regression curves for drainage and imbibition steps.

Figure 24. Evolution of measured radii of curvature R_1 for all drainage and imbibition steps.

The relationship between contact angles and radius of curvature is reflected by the point clouds and regression results presented in Fig. 25. Although the presented data show a lot of spread with regard to the measured radii of curvature and related contact angles, a certain trend between both measures can be found: with increasing contact angle, also the radius of curvature increases both for drainage and imbibition which is a plausible relationship if, for instance, one thinks of the geometric relationship of an ideal meniscus inside a capillary tube with varying contact angles and related radii of curvature.

Finally, also the capillary pressure can be calculated from interfacial tension and measured mean curvature (derived from the 2D radius of curvature) according to Eq. 4. This calculated capillary pressure is compared to the macroscopic matric suction before and after the CT scans in Fig. 26. A surprisingly close match of macroscopic matric suction and capillary pressure from measured radii of curvature can be noticed, leading to the assumption that macroscopic matric suction represents the averaged effect of the multitude of microscopic capillary menisci and their curvatures.
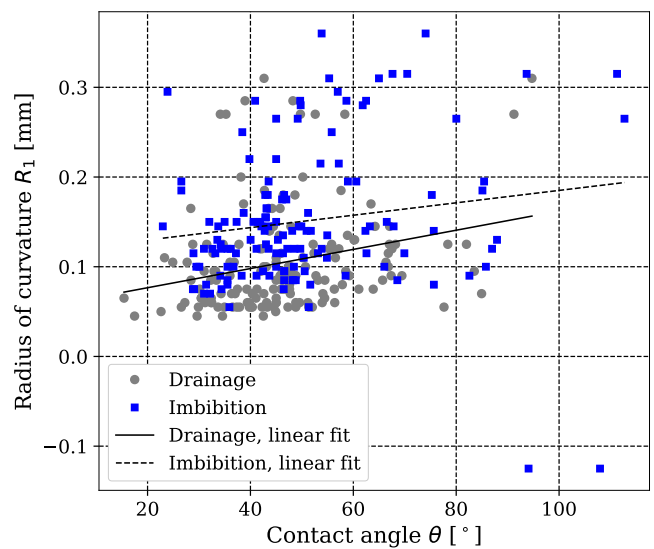
However, the macroscopic matric suction is slightly higher especially regarding its peaks. Note that the measurement of the smallest radii of curvature is limited by the voxel size of 0.01 mm/px. Therefore, very small radii, being associated with the highest capillary pressure, cannot be measured well, probably leading to the difference in the mean capillary pressure and macroscopic suction. Furthermore, the difference can be explained by the assumption of 2D conditions in our evaluation, neglecting the contribution of a second radius of curvature to mean curvature in 3D. Although maybe not applicable here, Jiang et al. [2017] explain differences between a "measured suction" and an "intrinsic suction" inside the soil based on theoretical thermodynamic considerations. According to their results, the intrinsic suction deviates from the measured suction and can be much higher than the measured suction. Interestingly, this is not the case based on our measurements where the suction calculated from interfacial curvatures is lower than the suction measured macroscopically.

Although capillary pressure is related to the radii of curvature, it can also be linked to the contact angles which themselves could be shown to be geometrically coupled to the radius of curvature. Linear regressions in Fig. 27 show an increase in capillary pressure with decreasing contact angle for both drainage and imbibition, which is intuitive. Please note that the data show multiple capillary pressures with the same magnitude for different contact angles. This is due to the fact that capillary pressure is calculated from radius of curvature discretised by voxel size and fitted into a meniscus which may also be represented by two different contact angles as shown in Fig. 30 in the Appendix.
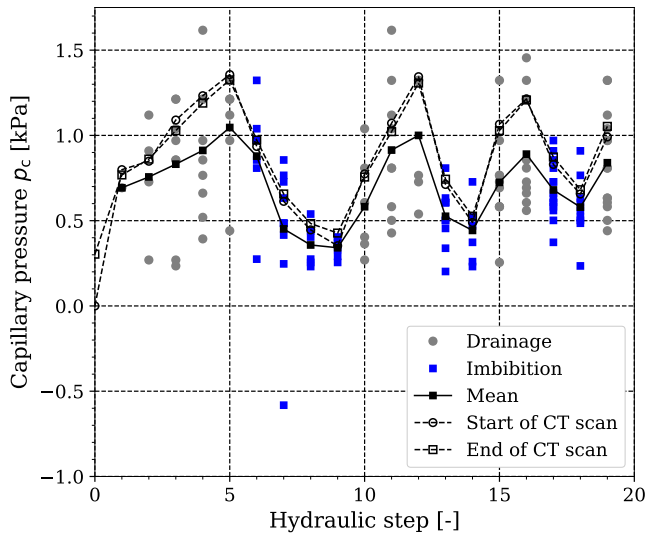
Figure 26. Evolution of capillary pressure, calculated from interfacial tension γ and 2D mean curvature $1/R_1$ (lone grey circles and blue squares and corresponding mean value indicated by black squares linked by a black line), compared to matric suction before and after a CT scan measured on a macroscopic level (indicated by circles and squares linked by dashed lines) for all drainage and imbibition steps.
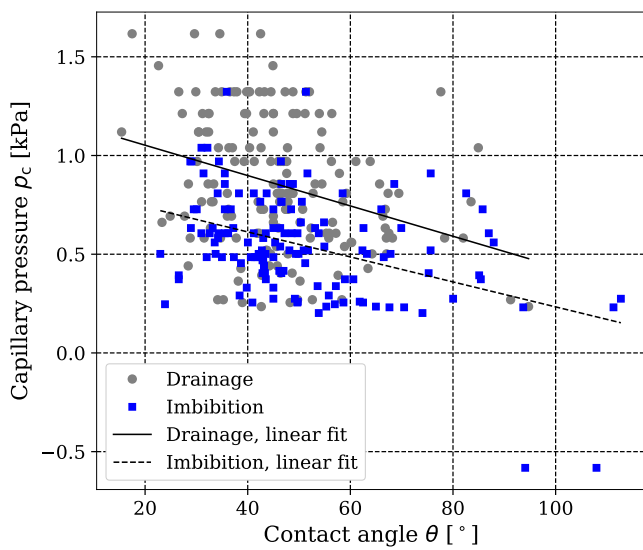

Figure 27. Calculated capillary pressure p_c plotted *vs.* the contact angles θ of the same meniscus with linear regression curves for drainage and imbibition steps.

3.3. Discrete analysis of grain displacements and pore-based drainage

Based on the DDIC analysis, interesting insights into hydro-mechanical coupling during prescribed drainage can be obtained. Fig. 36 and Fig. 37 in the Appendix juxtapose trinarised images and calculated grain displacements for two vertical slices through the full sand specimen for the

primary drainage path. A pronounced settlement of grains at the bottom of the specimen becomes visible already after the initial drainage step. Generally, the whole specimen seems to encounter very slight settlements rather homogeneously distributed over the specimen volume. For some grains, pronounced upward movements become visible as the surrounding pores are emptied. This shows that capillary action, going along with emerging water clusters and liquid bridges, can lift individual grains against gravity and thus is doing work, changing the overall energy balance inside the specimen.

A grain count of sand grains moving either downward or upward together with the number of contracting and dilating pores based on volumetric strain is shown in Fig. 38 in the Appendix for all hydraulic steps on the primary drainage path. Most grains are encountering settlement already early in the experiment, while a small portion of grains is lifted upward. The pronounced initial settlement of the sand grains is mainly due to a contraction of the filter paper at the specimen bottom during the first drainage step. On a volumetric basis, most pores show contractancy (positive volumetric strain based on the soil mechanics sign convention), while some pores are strained due to dilatancy, which is in accordance with the observed reduction of macroscopic void ratio during primary drainage.

With the help of pores defined based on the triangulation, linking the grain centres, pore scale hydraulic events have been statistically analysed and related to measured volumetric strain. Characterising each pore by its pore volume and degree of saturation, allows to investigate the drainage process on the pore scale as given in Fig. 28. In this subplot, the pore size distribution is plotted together with the median of pore-based degree of saturation in pores classified by their pore volume as well as the median of volumetric strain measured for each pore-containing tetrahedron for the hydraulic steps on the primary drainage path.

The pore size distribution in Fig. 28 (a) based on 25 bins is skewed to the left, indicating that small to medium-sized pores prevail. During the drainage steps, the number of smaller pores is slightly increasing, while apparently also very few larger pores are created. In the drainage process, shown in Fig. 28 (b), clear evidence is found for a drainage sequence, with larger pores being emptied first, which can be explained by their lower air entry capillary pressure. Starting with experimental step 1, slight reductions of median saturation are noticed. After drainage step 2, pores with a volume larger than 0.0045 mm^3 have been emptied irregularly, leaving pores with smaller pore volume still filled. The irregular emptying of larger pores is in accordance with the air fingering phenomenon observed for the first steps of primary drainage. For the consecutive hydraulic steps 3 to 5, a more steady relationship between median pore saturation and pore volume is found, indicating higher degrees of saturation only for the smallest pores where a higher capillary pressure retains the pore water.

Based on the evolution of median volumetric strain plotted *vs.* the middle of each pore volume bin in Fig. 28 (c), hydro-mechanical coupling effects on the pore level can be interpreted. The results reveal an increasing contractancy
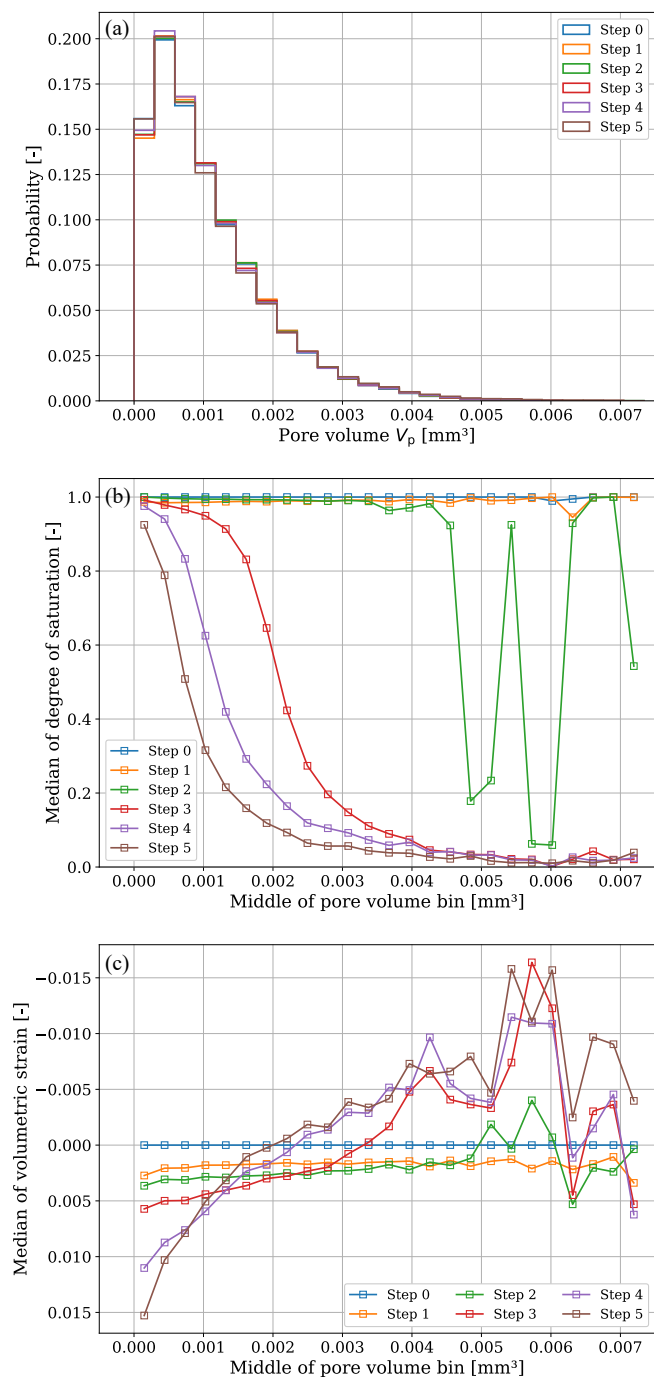
Open Geomechanics, 2022, article no. 5

Marius Milatz, Edward Andò, Gioacchino Viggiani & Serge Mora, *In situ X-ray CT imaging of transient water retention experiments with cyclic drainage and imbibition*

20

Figure 28. (a) Evolution of pore size distribution, (b) median of pore saturation and (c) volumetric strain in pores classified by pore size for primary drainage.

of the many smaller pores, while the much fewer larger pores tend to dilatant volumetric behaviour upon primary drainage. On both ends of pore sizes and degrees of saturation, the constraining impact of pore scale capillary effects is highlighted, with increasing suction and suction stress in the many saturated or close to saturated small pores leading to contractant behaviour. On the other hand, the fewer emptied larger pores show a dilatant behaviour, possibly due to the loss of constraining suction, *i.e.*, relaxation of suction stress, and due to the formation of liquid bridges.

4. Conclusion and outlook on further research

The transient *in situ* CT flow experiments presented in this contribution allow for interesting insights into processes in unsaturated granular media on the grain or pore scale. To our knowledge, for the first time a series of 3D CT images could be captured and analysed during a multitude of different consecutive drainage and imbibition cycles in a quasi automated imaging experiment with continuous measurement of the macroscopic WRC. Regarding the guiding questions of research, many results and answers could be derived from the experimental data which are summarised and discussed in the following.

1) Can the theories of microscopic origin of hysteresis be confirmed? Focusing on the microscopic origin of hysteresis, the measured CT data opens the door to the analysis of flow processes on the pore scale (although limited by coarse temporal resolution). Typical processes known from literature could be observed, *e. g.*, the effect of air fingering at air entry (see Fig. 13), leading to water first emptying larger pores in a drainage sequence, or the effect of air entrapment. Furthermore, an analysis of contact angles as well as radii of curvature measured for individual menisci has revealed contact angle hysteresis which also comes with hysteresis of radii of curvature. With matric suction being a function of the mean curvature, its hysteresis is also due to the hysteresis of shape of the menisci during drainage and imbibition. The macroscopic matric suction response could be shown to be closely related to the mean of the suction derived from interfacial tension and mean curvature. Furthermore, it could be shown that contact angle-hysteresis is a developing process. It takes some time upon a change of flow direction for the menisci to change shape. Very frequently, contact angles cannot develop freely because grain roughness or grain edges cause a pinning of the contact line.

2) Which phase distributions and fluid structures develop during cyclic drainage and imbibition? The cyclic drainage and imbibition as applied by forced flow in the presented experiments leads to a change of air and water clusters with an anticyclical pattern. After specimen preparation by pluviation of dry sand into water, many spherical air bubbles could be shown to be already present in the pores. During primary drainage, preferential paths of air fingers (larger pores are filled with air from the top of the specimen) and the cycling of degree of saturation lead to entrapped larger air clusters of irregular shape. The air cluster shape analysis indicates that further scanning paths obviously lead to more and more complex air ganglia inside the specimen. Both for air and water, very small separated cluster volumes dominate the cluster size distributions besides fewer larger connected clusters. A trend towards more air ganglia with complex shapes (characterised by low sphericity) and a reduction of the number of spherical air bubbles could be shown with increasing number of hydraulic cycles.

The phase distributions evaluated *vs.* specimen height in Fig. 14 indicate the influence of the applied boundary conditions as well as the formation of preferential air paths upon drainage, leading to more air at the bottom part of the

Open Geomechanics, 2022, article no. 5

Marius Milatz, Edward Andò, Gioacchino Viggiani & Serge Mora, *In situ X-ray CT imaging of transient water retention experiments with cyclic drainage and imbibition*

21

specimen where water is drained and imbibed through a porous filter. The macroscopic suction response with all its oscillations upon drainage could be shown to reflect the local microscopic air entry events which lead to a reduction of hydraulic contact of the water phase inside the specimen and the water underneath the filter where macroscopic suction is measured by a pore pressure sensor.

3) How do microscopic *capillary state variables*, such as the interfacial areas, the length of the contact line or contact angles as potential ingredients of effective stress, develop upon different hydraulic paths? Characteristic relationships of *capillary state variables*, such as the air-water interfacial and solid-water interfacial areas as well as the length of contact line, *vs.* local degree of saturation and macroscopic matric suction could be measured for many different hydraulic paths of the WRC. These "Soil Water Air Interface Characteristic Curves" show pronounced hysteresis when the interfacial areas or specific lengths of contact line are plotted *vs.* matric suction because matric suction itself is hysteretic *vs.* degree of saturation due to changing radii of curvature and contact angles upon drainage and imbibition. When shown *vs.* degree of saturation, the interfacial areas and specific lengths of contact line only show light hysteresis. As different authors have proposed the formulation of effective stress in unsaturated soils based on some of these interfaces *e. g.*, Gray et al. [2009], Nikooee et al. [2013], and Wang et al. [2019], the presented data could be applied to extend formulations for suction stress. This also holds true for the specific length of contact line along which interfacial tension is acting on the solid phase.

Including the measured capillary state variables in hydromechanical considerations, could also improve our understanding of the functional dependencies behind the WRC. As proposed by Hassanizadeh and Gray [1990, 1993], the interfacial properties could also be relevant to the hysteresis in the WRC. Based on the data presented in this study, it could be shown that the air-water interfacial area evolves in a 3D surface, when plotted *vs.* degree of saturation and matric suction. Although not presented in this contribution, the same holds true for the solid-water interfacial area and the specific length of contact line.

As potential experimental evidence for a changing suction stress during drainage and imbibition which is typically hard to measure directly, a "breathing" of the grain skeleton leading to a small reversible and cyclic change in void ratio could be observed showing a decrease in void ratio upon drainage and suction build up and an increase of void ratio upon imbibition and suction reduction. The DDIC analysis has confirmed that primary drainage is indeed accompanied by positive volumetric strain, *i. e.*, contractant behaviour, especially of the smaller pores. Furthermore, upward "grain jumps" due to capillary action could be quantitatively measured, representing another interesting aspect of hydro-mechanical coupling which requires further investigation. Although also slight local settlements at the specimen bottom have been measured, the local volumetric and pore-based observations might represent the direct effect of changing effective stress as influenced by changing interfaces and suction stress on the pore level.

In extension to existing effective stress formulations which include interfacial areas, *e. g.*, according to Gray et al. [2009], Lu et al. [2010], Nikooee et al. [2013], and Wang et al. [2019], we propose to derive effective stress from a combination of the solid-water interfacial area as well as the air-water interfacial area. While the solid-water interfacial area represents the wetted surface area where capillary pressure or suction acts on the grain surfaces, the air-water interfacial areas represent the surface areas of the menisci or capillary bridges in the cross section of which the interfacial tension leads to an additional force in between grains. The contribution of both effects, capillary pressure and interfacial tension, is already included in established capillary force models and could also be considered for future suction stress formulations.

To conclude, the presented data, that we will make available for further research, represents a single experimental data set of one material. Although, the data could be exploited in many ways, leading to interesting insights regarding the macroscopic WRC, more experiments on different granular materials are needed in the future. This would allow to further quantify the effects of grain shape as well as porosity on the measured interfacial area characteristics and other *capillary state variables*. Further questions to be answered refer to the influence of flow rate on the WRC which becomes transient or dynamic at higher flow rates and to the relaxation processes happening in the unsaturated specimens upon a stop of flow. Here, a faster image acquisition, as is already possible in synchrotron-based tomography, is needed. Furthermore, more experiments focusing on the influence of specimen size and boundary effects would be of interest.

Research data

The research data related to this article is published via the repository TUHH Open Research (TORE) in Milatz et al. [2022] and can be found via the following url: `https://doi.org/10.15480/336.4291`.

Conflicts of Interest

The authors see no potential conflicts of interest due to publishing of this paper. The complete review history is available online.

Acknowledgements

References

AlRatrout, A., Raeini, A. Q., Bijeljic, B., and Blunt, M. J. (2017). Automatic measurement of contact angle in pore-space images. *Advances in Water Resources*, 109:158–169.

Andrew, M., Bijeljic, B., and Blunt, M. J. (2014). Pore-scale contact angle measurements at reservoir conditions using X-ray microtomography. *Advances in Water Resources*, 68:24–31.

Armstrong, R. T., Porter, M. L., and Wildenschild, D. (2012). Linking pore-scale interfacial curvature to column-scale capillary pressure. *Advances in Water Resources*, 46:55–62.

ASTMD6836-16 (2016). *Standard Test Methods for Determination of the Soil Water Characteristic Curve for Desorption Using Hanging Column, Pressure Extractor, Chilled Mirror Hygrometer, or Centrifuge*. ASTM International.

Avizo 2019.3 (2019). User's guide Avizo software 2019. https://assets.thermofisher.com/TFS-Assets/MSD/Product-Guides/users-guide-avizo-software-2019.pdf. Accessed: 2022-07-09.

Bear, J. (1979). *Hydraulics of groundwater*. New York: Mc Graw-Hill (Mc Graw-Hill Series in Water Resources and Environmental Eng.).

Blunt, M. J. (2017). *Multiphase Flow in Permeable Media: A Pore-Scale Perspective*. Cambridge University Press.

Culligan, K. A., Wildenschild, D., Christensen, B. S. B., Gray, W. G., Rivers, M. L., and Tompson, A. F. B. (2004). Interfacial area measurements for unsaturated flow through a porous medium. *Water Resources Research*, 40.

de Gennes, P.-G., Brochard-Wyart, F., and Quéré, D. (2004). *Capillarity and Wetting Phenomena: Drops, Bubbles, Pearls, Waves*. Springer.

DFG PintPFS (2019). DFG Research Training Group GRK 2462: Processes in natural and technical Particle-Fluid-Systems (PintPFS). http://gepris.dfg.de/gepris/projekt/390794421?language=en. Accessed: 2019-04-29.

Diamantopoulos, E. and Durner, W. (2012). Dynamic nonequilibrium of water flow in porous media: A review. *Vadose Zone Journal*, 11.

FiJi (2022). FiJi (Fiji Is Just ImageJ), open-source image processing package for ImageJ. https://imagej.net/Fiji. Accessed: 2020-06-18.

Fredlund, D. G. and Rahardjo, H. (1993). *Soil mechanics for unsaturated soils*. John Wiley & Sons.

Gastal, E. S. L. and Oliveira, M. M. (2012). Adaptive manifolds for real-time high-dimensional filtering. *ACM Trans. Graph.*, 31(4).

Gray, W. G., Schrefler, B. A., and Pesavento, F. (2009). The solid phase stress tensor in porous media mechanics and the Hill–Mandel condition. *Journal of the Mechanics and Physics of Solids*, 57:539–554.

Haines, W. B. (1930). Studies in the physical properties of soil: V. The hysteresis effect in capillary properties and the modes of moisture distribution associated therewith. *Journal of Agricultural Science*, 20:97–116.

Hassanizadeh, S. M., Celia, M. A., and Dahle, H. K. (2002). Dynamic effect in the capillary pressure-saturation relationship and its impacts on unsaturated flow. *Vadose Zone Journal*, 1:38–57.

Hassanizadeh, S. M. and Gray, W. G. (1990). Mechanics and thermodynamics of multiphase flow in porous media including interphase boundaries. *Advances in Water Resources*, 13:169–186.

Hassanizadeh, S. M. and Gray, W. G. (1993). Thermodynamic basis of capillary pressure in porous media. *Water Resources Research*, 29:3389–3405.

Higo, Y., Morishita, R., Kido, R., Khaddour, G., and Salager, S. (2015). Local water-retention behaviour of sand during drying and wetting process observed by micro x-ray tomography with trinarisation. *Japanese Geotechnical Society Special Publication*, 2:635–638.

Jiang, Y., Einav, I., and Liu, M. (2017). A thermodynamic treatment of partially saturated soils revealing the structure of effective stress. *Journal of the Mechanics and Physics of Solids*, 100:131–146.

Jones, A. C., Arns, C. H., Sheppard, A. P., Hutmacher, D. W., Milthorpe, B. K., and Knackstedt, M. A. (2007). Assessment of bone ingrowth into porous biomaterials using micro-ct. *Biomaterials*, 28.

Khaddour, G. (2015). *Multi-scale characterisation of the hydro-mechanical behaviour of unsaturated sand: water retention and triaxial responses*. Ph.d. thesis, Laboratoire 3SR, Université Grenoble Alpes.

Khaddour, G., Riedel, I., Andò, E., Charrier, P., Bésuelle, P., Desrues, J., Viggiani, G., and Salager, S. (2018). Grain-scale characterization of water retention behaviour of sand using X-ray CT. *Acta Geotechnica*.

Kido, R., Higo, Y., Takamura, F., Morishita, R., and Khaddour, G. (2020). Morphological transitions for pore water and pore air during drying and wetting processes in partially saturated sand. *Acta Geotechnica*, 15:1745–1761.

Kim, F. H., Penumadu, D., Gregor, J., and Kardjilov, N. (2013). High-Resolution Neutron and X-Ray Imaging of Granular Materials. *Journal of Geotechnical and Geoenvironmental Engineering*, 139.

Lins, Y. (2009). *Hydro-mechanical properties of partially saturated sand*. Dissertation, Faculty of Civil Engineering, University Bochum.

Lu, N., Godt, J. W., and Wu, D. T. (2010). A closed-form equation for effective stress in unsaturated soil. *Water Resources Research*, 46.

Manahiloh, K. N. and Meehan, C. L. (2017). Determining the soil water characteristic curve and interfacial contact angle from microstructural analysis of x-ray ct images. *Journal of Geotechnical and Geoenvironmental Engineering*, 143.

Milatz, M. (2015). An experimental method to study the drying-wetting behaviour of a sand. In Chen, Z., Wei, C., Sun, D., and Xu, X., editors, *Proc. of 6th Asia-Pacific Conference on Unsaturated Soils (AP-UNSAT 2015), Guilin, China*, pages 211–216.

Milatz, M. (2020). An automated testing device for continuous measurement of the hysteretic water retention curve of granular media. *Acta Geotechnica*.

Open Geomechanics, 2022, article no. 5
Marius Milatz, Edward Andò, Gioacchino Viggiani & Serge Mora, *In situ X-ray CT imaging of transient water retention experiments with cyclic drainage and imbibition*

23

Milatz, M., Andò, E., and Viggiani, G. (2022). *Data from in situ X-ray CT imaging of transient water retention experiments with cyclic drainage and imbibition.* TUHH Open Research (TORE), Hamburg University of Technology.

Milatz, M., Törzs, T., and Grabe, J. (2018a). Investigation of transient effects on the soil-water characteristic curve of different granular soils. In Ng, C. W. W., Leung, A. K., Chiu, A. C. F., and Zhou, C., editors, *Proc. of 7th International Conference on Unsaturated Soils (UNSAT 2018)*, volume 1, pages 355–360.

Milatz, M., Törzs, T., Nikooee, E., Hassanizadeh, S. M., and Grabe, J. (2018b). Theoretical and experimental investigations on the role of transient effects in the water retention behaviour of unsaturated granular soils. *Geomechanics for Energy and the Environment*, 15:54–64.

Mirzaei, M. and Das, D. B. (2013). Experimental investigation of hysteretic dynamic effect in capillary pressure-saturation relationship for two-phase flow in porous media. *AIChE Journal*, 59:3958–3974.

Nikooee, E., Habibagahi, G., Hassanizadeh, S. M., and Ghahramani, A. (2013). Effective stress in unsaturated soils: A thermodynamic approach based on the interfacial energy and hydromechanical coupling. *Transport in Porous Media*, 96:369–396.

Peters, A. and Durner, W. (2008). Simplified evaporation method for determining soil hydraulic properties. *Journal of Hydrology*, 356:147–162.

Porter, M. L., Schaap, M. G., and Wildenschild, D. (2009). Lattice-boltzmann simulations of the capillary pressure-saturation-interfacial area relationship for porous media. *Advances in Water Resources*, 32:1632–1640.

Schlüter, S., Berg, S., Rücker, M., Armstrong, R. T., Vogel, H.-J., Hilfer, R., and Wildenschild, D. (2016). Pore-scale displacement mechanisms as a source of hysteresis for two-phase flow in porous media. *Water Resources Research*, 52:2194–2205.

Stamati, O., Andò, E., Roubin, E., Cailletaud, R., Wiebicke, M., Pinzon, G., Couture, C., Hurley, R. C., Caulk, R., Caillerie, D., Matsushima, T., Bésuelle, P., Bertoni, F., Arnaud, T., Laborin, A. O., Rorato, R., Sun, Y., Tengattini, A., Okubadejo, O., Colliat, J.-B., Saadatfar, M., Garcia, F. E., Papazoglou, C., Vego, I., Brisard, S., Dijkstra, J., and Birmpilis, G. (2020). 'spam': Software for practical analysis of materials. *Journal of Open Source Software*, 5(51):2286.

Tengattini, A., Lenoir, N., Andò, E., and Viggiani, G. (2021). Neutron imaging for geomechanics: A review. *Geomechanics for Energy and the Environment*, 27.

Thakur, M. M., Penumadu, D., and Bauer, C. (2020). Capillary suction measurements in granular materials and direct numerical simulations using X-ray computed tomography microstructure. *Journal of Geotechnical and Geoenvironmental Engineering*, 146.

Tuller, M. and Or, D. (2001). Hydraulic conductivity of variably saturated porous media: Film and corner flow in angular pore space. *Water Resources Research*, 37:1257–1276.

Tuller, M., Or, D., and Dudley, L. M. (1999). Adsorption and capillary condensation in porous media: Liquid retention and interfacial configurations in angular pores. *Water Resources Research*, 35:1949–1964.

UMS (2018). HYPROP operation manual. `http://library.metergroup.com/Manuals/UMS/Hyprop_Manual.pdf`. Accessed: 2020-05-18.

Vanapalli, S. K., Nicotera, M. V., and Sharma, R. S. (2008). Axis translation and negative water column techniques for suction control. *Geotechnical and Geological Engineering*, 26 (6):645–660.

Viggiani, G., Andò, E., Takano, E., and Santamarina, J. C. (2015). Laboratory X-ray Tomography: A Valuable Experimental Tool for Revealing Processes in Soils. *Geotechnical Testing Journal*, 38.

Wadell, H. (1935). Volume, shape and roundness of quartz particles. *Journal of Geology*, 43:250–280.

Wang, J., Lambert, P., De Kock, T., Cnudde, V., and François, B. (2019). Investigation of the effect of specific interfacial area on strength of unsaturated granular materials by X-ray tomography. *Acta Geotechnica*, 14:1545–1559.

Wildenschild, D., Hopmans, J. W., Kent, A. J. R., and Rivers, M. L. (2005). Quantitative analysis of flow processes in a sand using synchrotron-based x-ray microtomography. *Vadose Zone Journal*, 4:112–126.

Wildenschild, D., Hopmans, J. W., Vaz, C. M. P., Rivers, M. L., Rikard, D., and Christensen, B. S. B. (2002). Using x-ray computed tomography in hydrology: systems, resolutions, and limitations. *Journal of Hydrology*, 267:285–297.

Zhuang, L. (2017). *Advanced Theories of Water Infiltration and Redistribution in Porous Media; Experimental Studies and Modeling*. PhD thesis,, Utrecht University, Utrecht, Netherlands.

Open Geomechanics, 2022, article no. 5

Marius Milatz, Edward Andò, Gioacchino Viggiani & Serge Mora, *In situ X-ray CT imaging of transient water retention experiments with cyclic drainage and imbibition*

24

5. Appendix

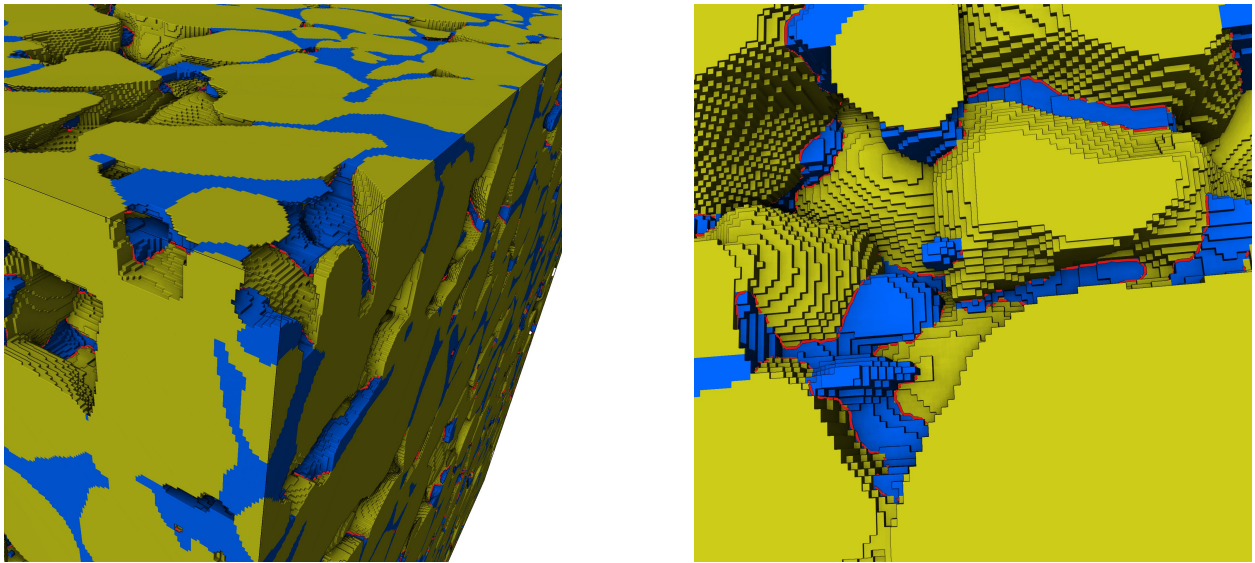## Measurement of the 3D contact line

Figure 29. Visualisation of the 3D contact line in a cubic subvolume containing Hamburg Sand and water at the lowest degree of saturation after primary drainage with the contact lines highlighted in red colour. Zoom onto one corner of the subvolume (left) and into a pore (right). Note that contact line segments touching the bounding box to exterior of the subvolume are not counted.

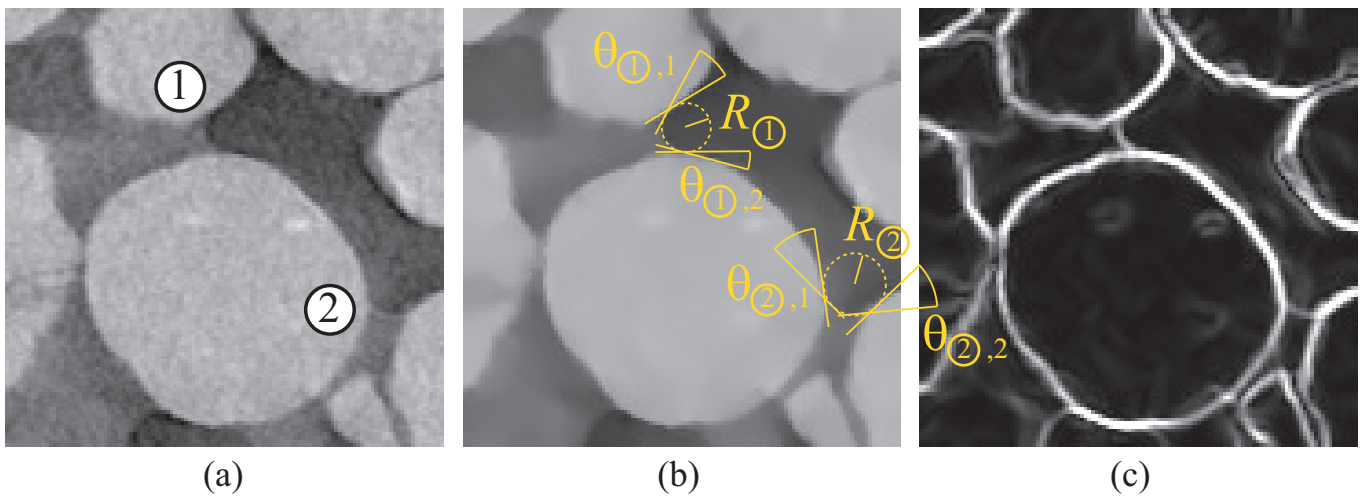## Measurement of contact angles and radii of curvature

Figure 30. Procedure of manual measurement of contact angles and radii of curvature of selected capillary menisci in Hamburg Sand from 2D images with 120×120 px. (a) Identification of two menisci (labelled 1 and 2) in greyscale image, (b) measurement using inscribed circles and an angle tool in a filtered image and (c) Sobel filtered image for edge detection as a further help.

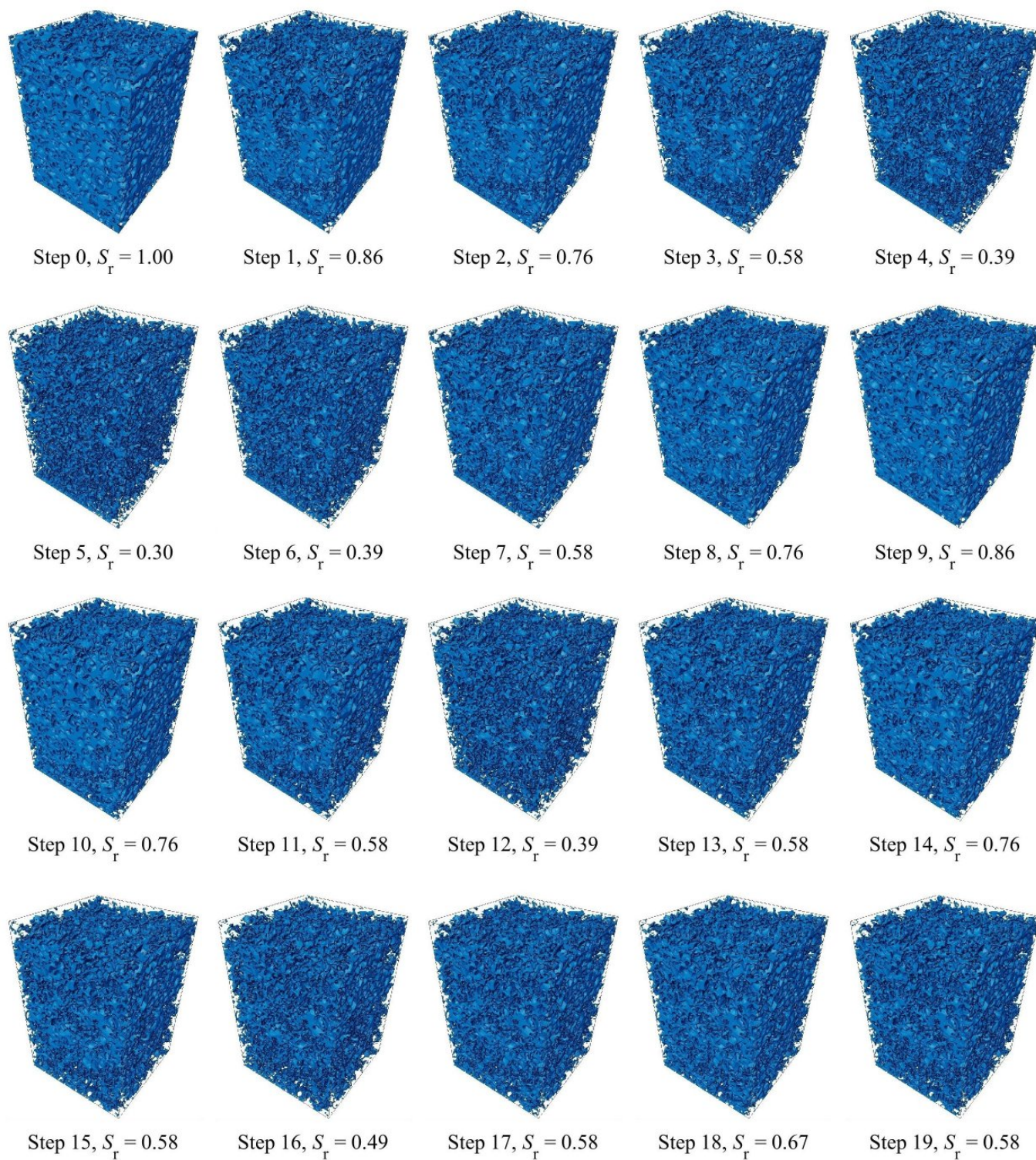**Visualisation of the water phase during cyclic drainage and imbibition**

Step 0, $S_r = 1.00$ Step 1, $S_r = 0.86$ Step 2, $S_r = 0.76$ Step 3, $S_r = 0.58$ Step 4, $S_r = 0.39$

Step 5, $S_r = 0.30$ Step 6, $S_r = 0.39$ Step 7, $S_r = 0.58$ Step 8, $S_r = 0.76$ Step 9, $S_r = 0.86$

Step 10, $S_r = 0.76$ Step 11, $S_r = 0.58$ Step 12, $S_r = 0.39$ Step 13, $S_r = 0.58$ Step 14, $S_r = 0.76$

Step 15, $S_r = 0.58$ Step 16, $S_r = 0.49$ Step 17, $S_r = 0.58$ Step 18, $S_r = 0.67$ Step 19, $S_r = 0.58$

Figure 31. Cyclic drainage and imbibition on a subvolume of $800\,\text{px} \times 800\,\text{px} \times 1145\,\text{px}$ ($8\,\text{mm} \times 8\,\text{mm} \times 11.45\,\text{mm}$). Reconstructed water volumes (blue). Step 0 indicates the water-saturated initial specimen state. Hydraulic steps and macroscopic degree of saturation according to Fig. 10.

Open Geomechanics, 2022, article no. 5

Marius Milatz, Edward Andò, Gioacchino Viggiani & Serge Mora, *In situ X-ray CT imaging of transient water retention experiments with cyclic drainage and imbibition*

26

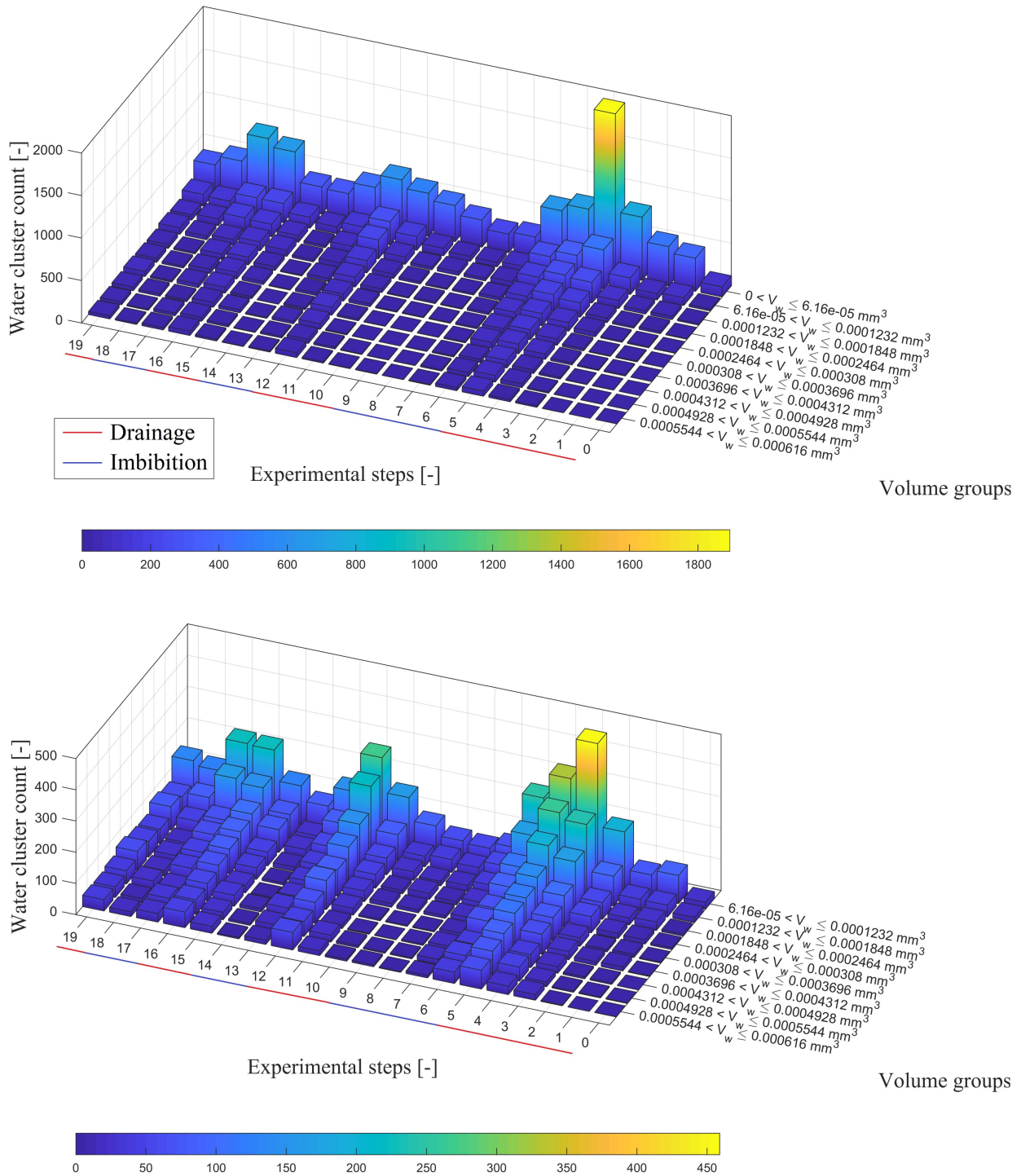# 3D histograms of the water and air cluster analysis

Figure 32. Histograms showing the evolution of water cluster count in different volume groups. The maximum water cluster volume included is the second largest cluster of the initial configuration with a volume of 0.000616 mm^3.
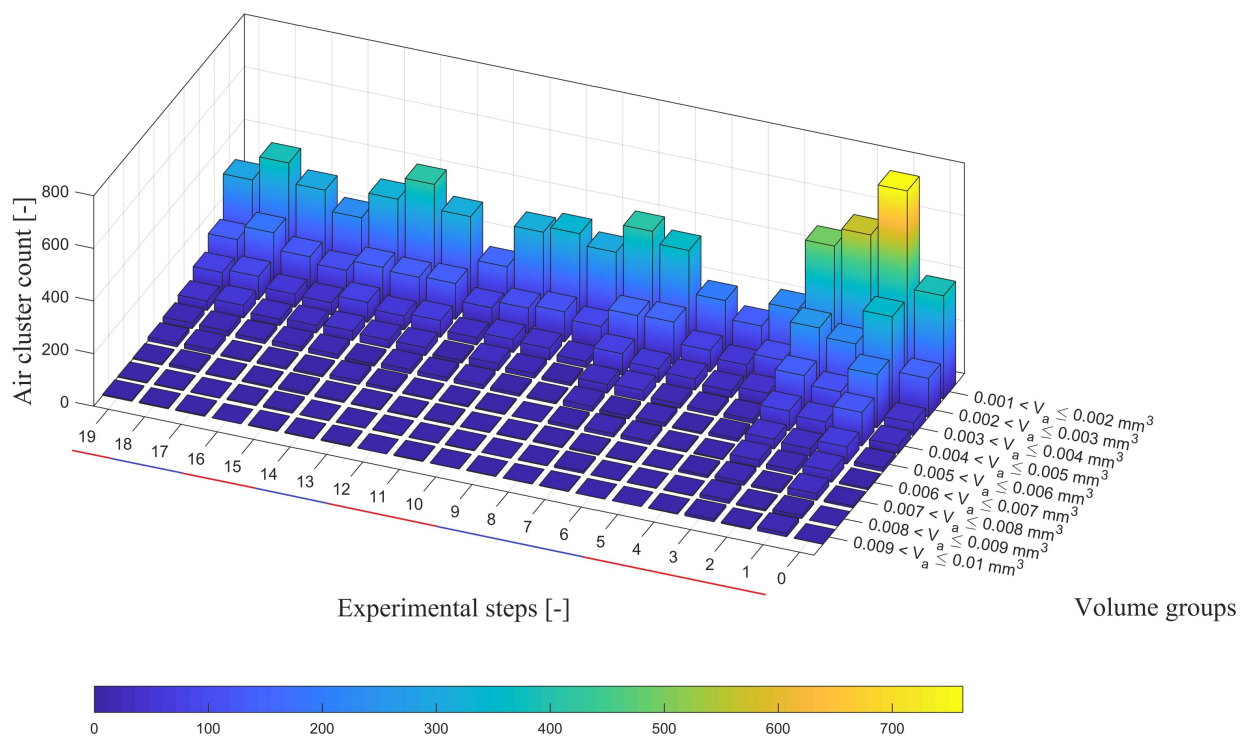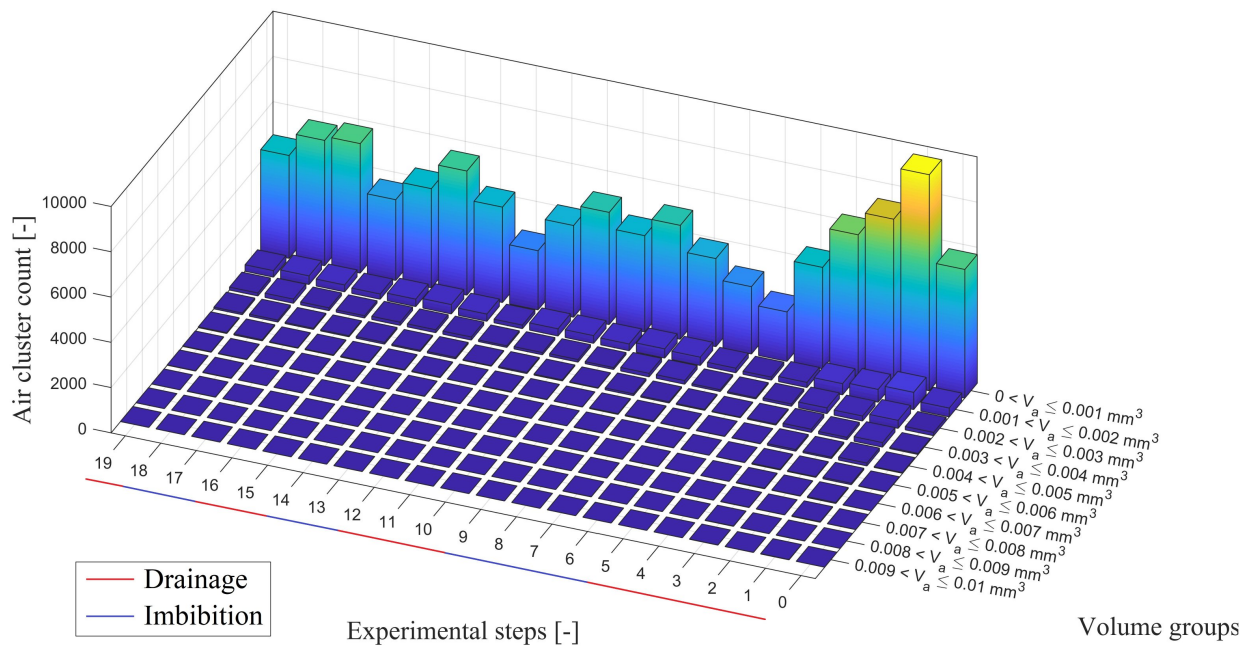
Open Geomechanics, 2022, article no. 5

Marius Milatz, Edward Andò, Gioacchino Viggiani & Serge Mora, *In situ X-ray CT imaging of transient water retention experiments with cyclic drainage and imbibition*

27

Figure 33. Histograms showing the evolution of air cluster count in different volume groups. The maximum air cluster volume included is 0.01 mm^3.
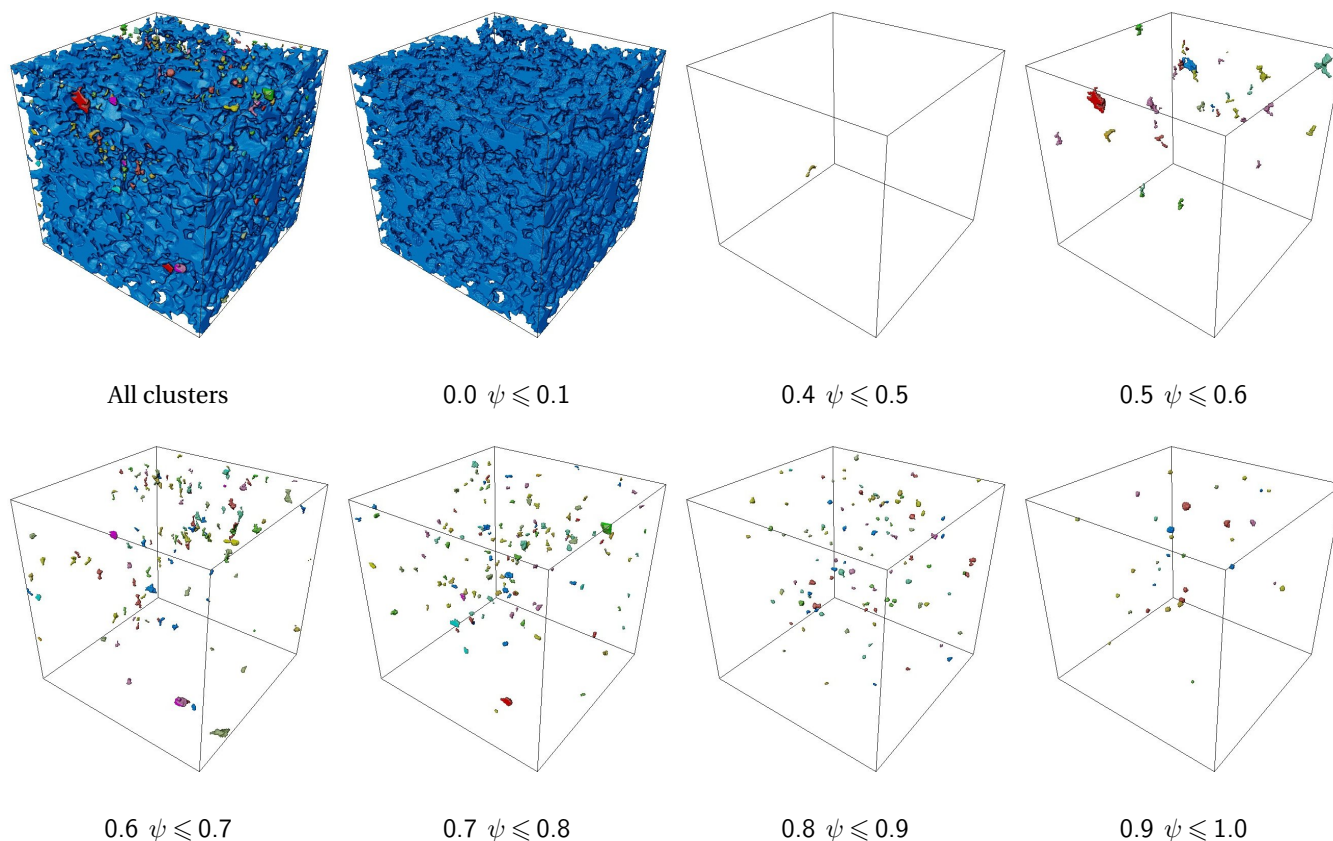
Air clusters as classified by sphericity ψ

All clusters	$0.0\ \psi \leqslant 0.1$	$0.4\ \psi \leqslant 0.5$	$0.5\ \psi \leqslant 0.6$
$0.6\ \psi \leqslant 0.7$	$0.7\ \psi \leqslant 0.8$	$0.8\ \psi \leqslant 0.9$	$0.9\ \psi \leqslant 1.0$

Figure 34. 3D visualisations of labelled air cluster volumes classified by their sphericity ψ in a central subvolume of 800 px $\times$ 800 px $\times$ 800 px from CT data after primary drainage. Air clusters with a volume larger than 0.0005 mm^3 are shown. Empty groups classified by ψ are omitted.

Relationship between air-water interfacial area, degree of saturation, and matric suction

Regarding the discussion on a unique water retention curve and its dependence on other capillary state variables, the 3D plot in Fig. 35 has been obtained, exemplarily including the measured air-water interfacial area.
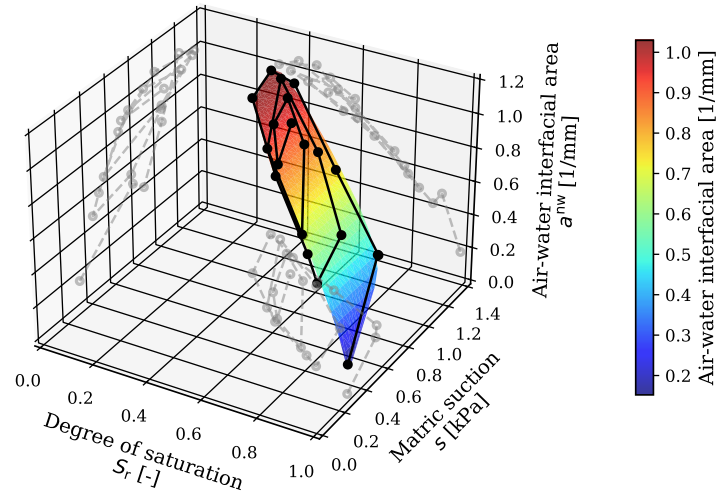

Figure 35. 3D plot of air-water interfacial area *vs.* degree of saturation and matric suction (suction measurements after each scan) based on data from the *in situ* CT experiments, including the projections of all inter-relationships (grey) and a 3D surface fitted to the data points to highlight the position of the data in a plane with good approximation.

The 3D surface area in Fig. 35 has been fitted based on a quartic polynomial surface function according to Eq. 8.

$$a^{\text{nw}} = aS_{\text{r}} + bS_{\text{r}}^2 + cS_{\text{r}}^3 + dS_{\text{r}}^4 + es + fs^2 + gs^3 + hs^4 + i, \tag{8}$$

with the fitting parameters summarised in table 4.

Table 4. Fitting parameters for the surface fitted to the data presented in Fig. 35.

a	b	c	d	e	f	g	h	i
8.197e+00	-2.265e+01	2.514e+01	-1.067e+01	-1.690e-02	4.039e-04	3.640e-04	-2.789e-05	3.392e-02

Open Geomechanics, 2022, article no. 5
Marius Milatz, Edward Andò, Gioacchino Viggiani & Serge Mora, *In situ X-ray CT imaging of transient water retention experiments with cyclic drainage and imbibition*

30

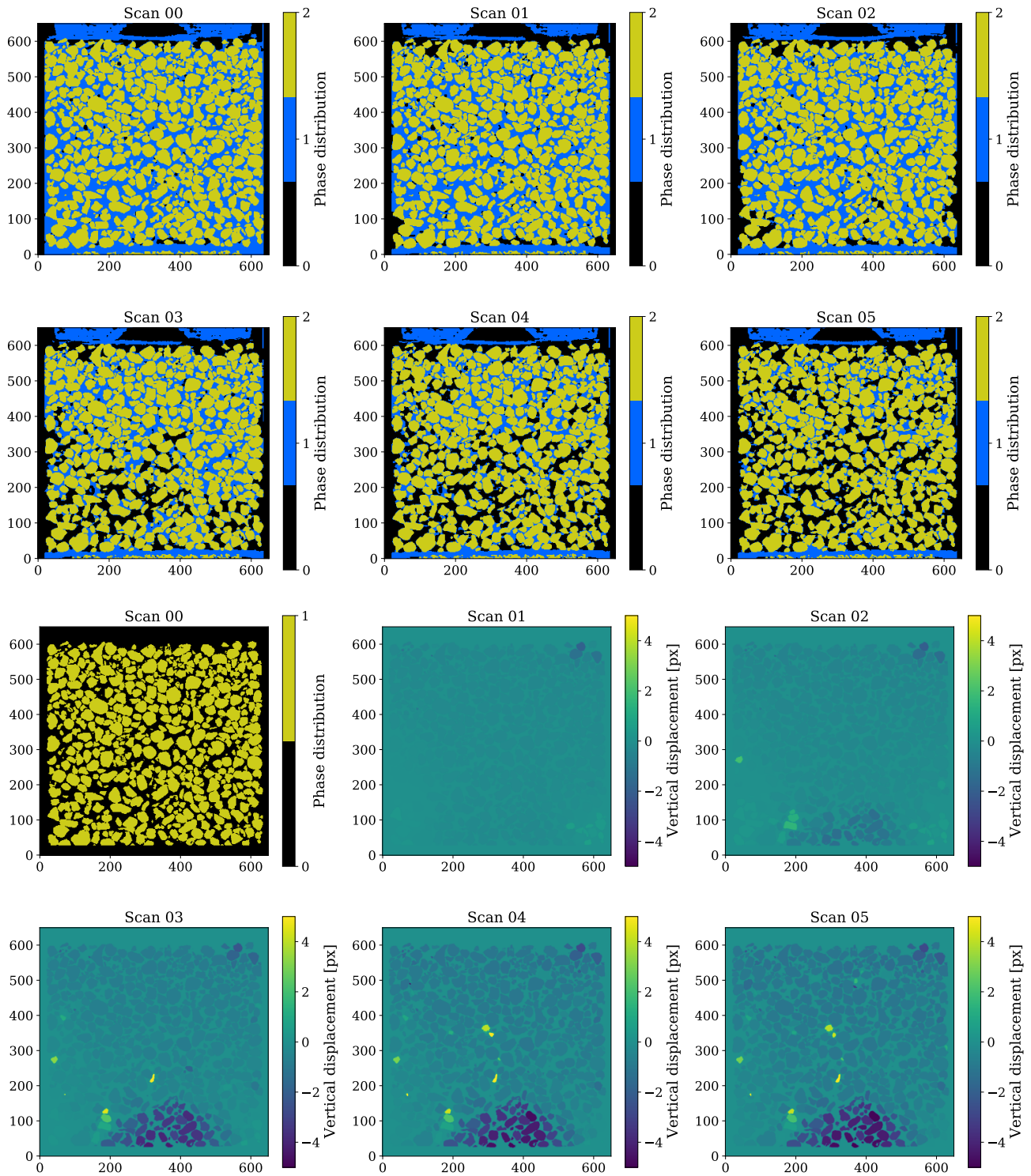# Results of grain kinematics and pore drainage analysis

Figure 36. Evolution of phase distribution in the trinarised images (top) and corresponding vertical grain displacements (bottom) for the initial state (Scan 00) and five hydraulic steps (Scans 01–05) during primary drainage (view in x-direction).
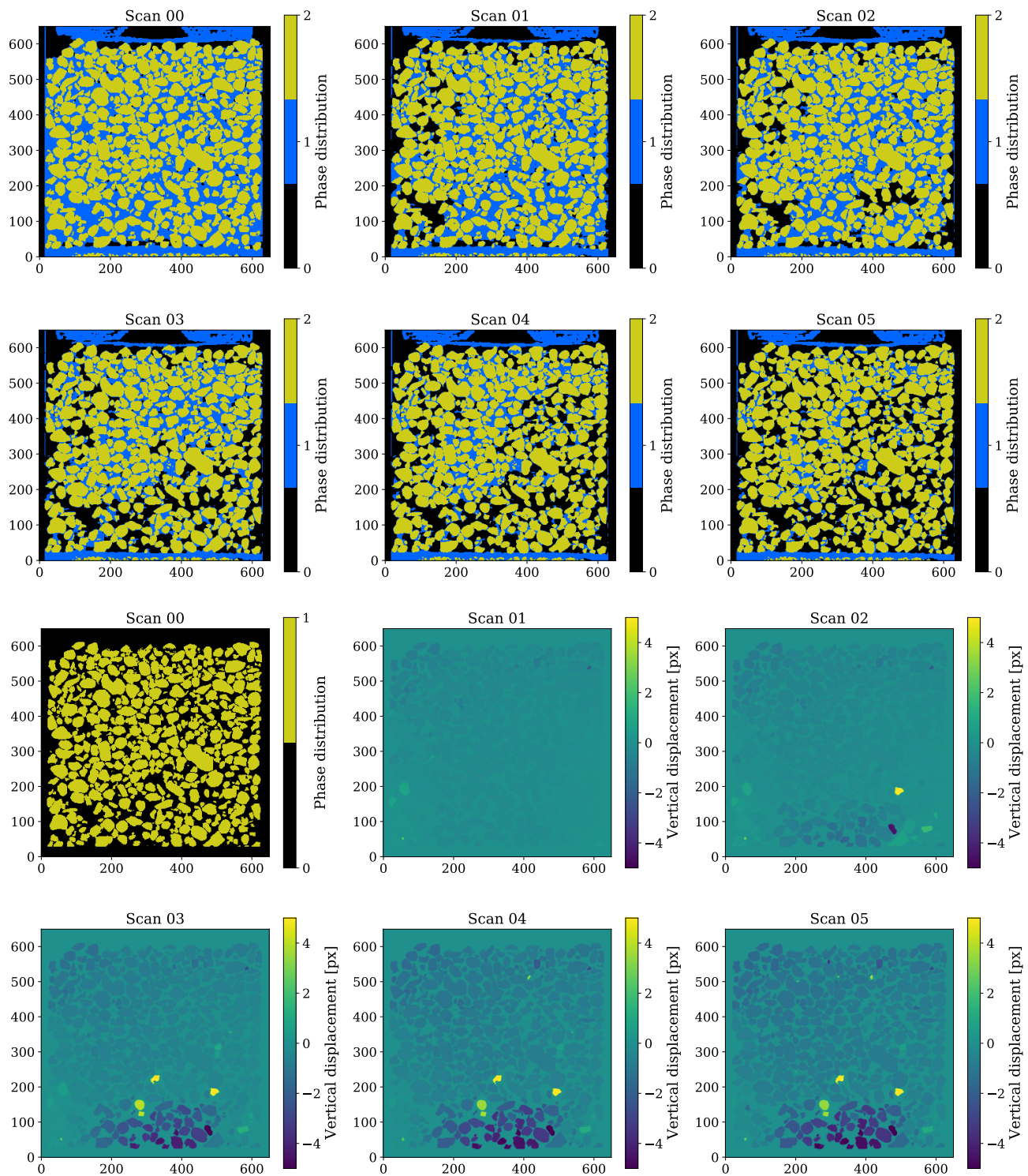
Open Geomechanics, 2022, article no. 5

Marius Milatz, Edward Andò, Gioacchino Viggiani & Serge Mora, *In situ X-ray CT imaging of transient water retention experiments with cyclic drainage and imbibition*

31

Figure 37. Evolution of phase distribution in the trinarised images (top) and corresponding vertical grain displacements (bottom) for the initial state (Scan 00) and five hydraulic steps (Scans 01–05) during primary drainage (view in y-direction).
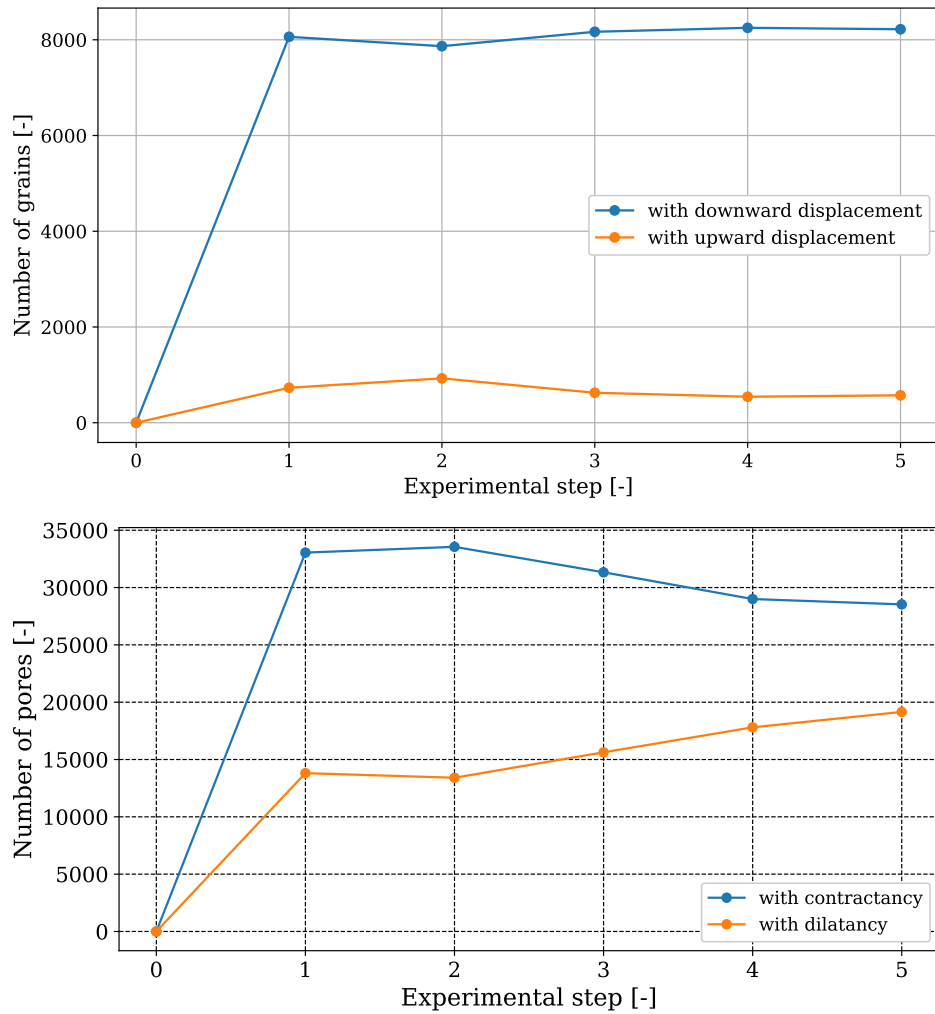
Figure 38. Number of sand grains moving downward or upward (top) and number of contractant or dilatant pores (bottom) during primary drainage.